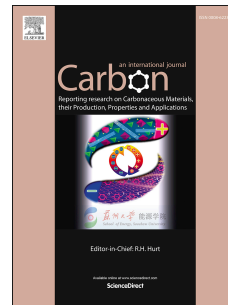


Journal Pre-proof

Switchable and Simultaneous Spatiotemporal Analog Computing with Computational Graphene-based Multilayers

Ali Momeni, Kasra Rouhi, Romain Fleury



PII: S0008-6223(21)00973-8

DOI: <https://doi.org/10.1016/j.carbon.2021.10.001>

Reference: CARBON 16699

To appear in: *Carbon*

Received Date: 30 April 2021

Revised Date: 23 August 2021

Accepted Date: 1 October 2021

Please cite this article as: A. Momeni, K. Rouhi, R. Fleury, Switchable and Simultaneous Spatiotemporal Analog Computing with Computational Graphene-based Multilayers, *Carbon*, <https://doi.org/10.1016/j.carbon.2021.10.001>.

This is a PDF file of an article that has undergone enhancements after acceptance, such as the addition of a cover page and metadata, and formatting for readability, but it is not yet the definitive version of record. This version will undergo additional copyediting, typesetting and review before it is published in its final form, but we are providing this version to give early visibility of the article. Please note that, during the production process, errors may be discovered which could affect the content, and all legal disclaimers that apply to the journal pertain.

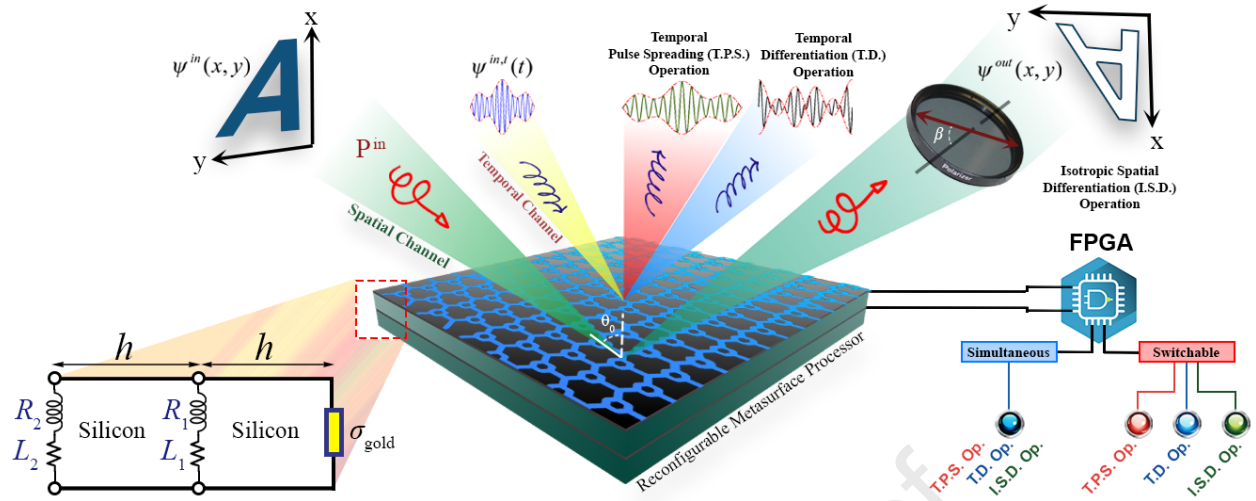
© 2021 The Author(s). Published by Elsevier Ltd.

Ali Momeni : Conceptualization, Methodology, Software, Validation, Formal analysis, Investigation, Data curation, Writing, Visualization

Kasra Rouhi : Methodology, Software, Validation, Formal analysis, Data curation, Writing, Visualization

Romain Fleury : Writing – Review and Editing, Supervision, Funding acquisition

Journal Pre-proof



Switchable and Simultaneous Spatiotemporal Analog Computing with Computational **Graphene-based Multilayers**

Ali Momeni^a, Kasra Rouhi^b and Romain Fleury^{a,*}

^aLaboratory of Wave Engineering, School of Electrical Engineering, Swiss Federal Institute of Technology in Lausanne (EPFL), Lausanne, Switzerland

^bSchool of Electrical Engineering, Iran University of Science and Technology, Tehran, Iran.

ARTICLE INFO

Keywords:

Graphene

multilayers

Spatiotemporal computing

Wave-based analog computing

ABSTRACT

In the past few years, analog computing has experienced rapid development but mostly for a single function. Motivated by parallel space-time computing and miniaturization, we show that reconfigurable graphene-based **multilayers** offer a promising path towards spatiotemporal computing with integrated functionalities by properly engineering both spatial- and temporal-frequency responses. This paper employs a tunable graphene-based **multilayers** to enable analog signal and image processing in both space and time by tuning the external bias. In the first part of the paper, we propose a switchable analog computing paradigm in which the proposed **multilayers** can switch among defined performances by selecting a proper external voltage for graphene monolayers. Spatial isotropic differentiation and edge detection in the spatial channel and first-order temporal differentiation and **multilayers**-based phaser with linear group-delay response in the temporal channel are demonstrated. In the second section of the paper, simultaneous and parallel spatiotemporal analog computing is demonstrated. The proposed **multilayers** processor has almost no static power consumption due to its floating-gate configuration. The spatial- and temporal-frequency transfer functions (TFs) are engineered using a transmission line (TL) model, and the obtained results are validated with full-wave simulations. Our proposal will enable real-time parallel spatiotemporal analog signal and image processing.

1. Introduction

Digital signal processors are widely used to accomplish a large variety of computational tasks. Despite their flexibility, they come with several drawbacks, such as significant power consumption, restricted processing speed, and incompatibility with high-frequency operation due to the technological limitations of current analog-to-digital converters [63]. The recent theoretical and manufacturing progress in the field of artificial photonic materials, e.g., photonic crystals or metamaterials, has inspired a return of the old paradigm of analog-based computing by leveraging low-loss structures that can process signals carried by light as it propagates through them. Optical analog signal processing could allow, in principle, for real-time, ultrafast, low energy consumption, and parallel processing [51, 2].

Recently proposed schemes for wave-based analog com-

*Corresponding author. Tel: +41 21 693 56 88. E-mail: ro-main.fleury@epfl.ch (Romain Fleury)
ORCID(s):

puting can be classified into two main categories, depending on whether they perform the processing operation in the spatial or temporal domain. On the one hand, spatial computing processes information encoded in the spatial dependency of an electromagnetic field, such as its intensity profile. Among the most popular techniques, the use of a 4-F correlator, which operates with two lenses performing Fourier transforms surrounding a spatial frequency filter, has found many applications in Fourier optics, and was recently miniaturized using metamaterials and **graphene-based multilayers**. Another known method for spatial processing is the transfer function (TF) method [51]. In the latter, the angular response of the system is designed in real space, such that it emulates a specific TF corresponding to a given linear mathematical operation. This method is potentially more compact as it avoids the use of components to take a Fourier transform and large propagation paths, leading to devices down or below the size of the wavelength, based e.g. on

photonic crystal slabs [16], plasmonic surfaces [74], metasurfaces [37, 1, 40, 4, 38, 5], photonic spin Hall insulators [20], inverse-designed metastructures [12], topological wave insulators [62] or deep-learning approaches [36]. In optics, one- and two-dimensional image edge detection has been demonstrated using various platforms, such as optical metasurfaces [69, 72, 70, 24] and surface plasmons [74]. On the other hand, temporal analog signal processing systems manipulate signals in the time domain with a dispersive structure, called a phaser [41]. Modern analog optical temporal computing dates back to the work of Pandian and Seraji [44], in which the transient optical response of a fiber ring resonator is investigated and proposed for several applications, including optical pulse differentiation, integration, and delay. In recent years, various architectures have been reported for temporal processing, such as differentiators [23, 27, 33], integrators [14, 33], and equation solvers [60, 55]. Despite all these advances, computing devices capable of performing both temporal and spatial operations, either sequentially or simultaneously, have been left largely unexplored. Spatiotemporal processors can exploit a much higher number of degrees of freedom, which could potentially be beneficial to analog computing systems, by enlarging the channel bandwidth and parallel operation capability.

For switching between spatial, temporal, or spatio-temporal operation modes, externally tunable electromagnetic properties, such as the amplitude and phase of the reflection, is ideal. This can be achieved using a tunable active metamaterial/metasurface [22, 28]. Up to now, a variety of strategies have been proposed to design reconfigurable metamaterial/metasurfaces. Two-dimensional materials such as graphene, that exhibit a plethora of exceptional electromagnetic and photonic properties, have attracted tremendous attention as promising candidates for compact switchable devices. The

relaxation time of the excited carriers in graphene is in the picosecond range, which is interesting for ultrafast wave manipulation [56]. The arbitrary control of graphene's complex surface conductivity can also be continuously tuned by manipulating its Fermi level by electric gating or photo-induced doping, which directly provides efficient real-time control of reflected/transmitted waves [25]. Accordingly, Fermi level control through external biasing or chemical doping has enabled the integration of THz devices with flexible substrates [34]. The strong interaction of graphene with electromagnetic fields has been leveraged in impressive applications such as wideband absorbers [47, 54, 43], polarization rotators [65], near field imaging [30], nanoantennas [61], biosensors [58], and THz wave devices [49, 68, 39, 8].

In this work, we propose an appealing power-efficient opportunity to perform analog signal and image processing in both time and space domains without resorting to intricate solutions involving various devices and bulky Fourier lenses. Systematically speaking, here, we consider a 2×2 multiple-input and multiple-output (MIMO) graphene **multilayers** processor in which the two inputs/outputs correspond to temporal and spatial processing channels. We use the tunability of graphene to construct a planar dual space-time processor that can perform space and time-domain signal processing tasks sequentially or at the same time. The **graphene-based multilayers** processor can accomplish an isotropic spatial differentiation operation for edge detection of a spatially encoded image. Simultaneously, in the temporal channel, the **graphene-based multilayers** processor can serve as a differentiator or **graphene-based multilayers** phaser for temporal pulse spreading when the input signal has a time variation. We confirm that the graphene-based **multilayers** can be tuned to enable analog signal processing in both space and time domains by changing the external voltage. In such

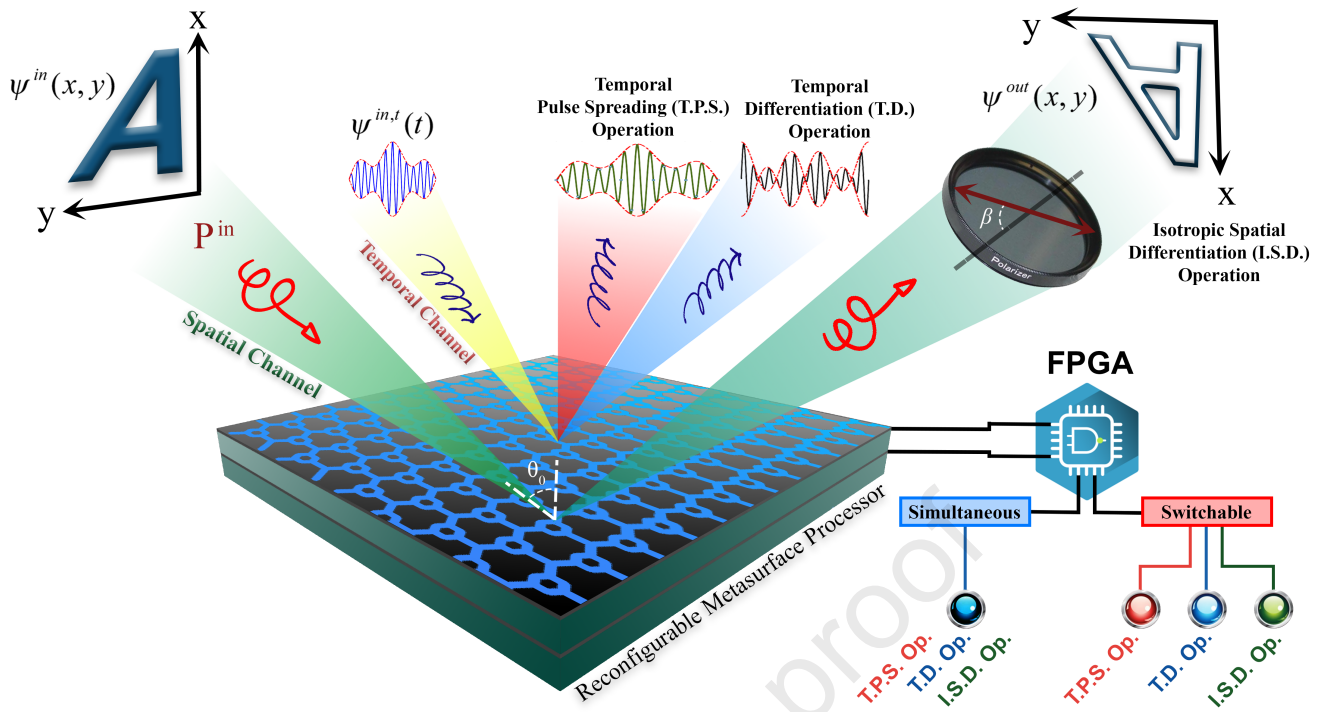


Figure 1: Schematic of the proposed spatiotemporal **graphene-based multilayers** processor with different functionalities. We can switch between different functionality states by controlling an external voltage via an FPGA processor.

a design, the graphene monolayer can capture the electrons tunneling from a positive external bias, but cannot release them after releasing the DC voltage because it is electrically isolated from the biasing electrodes [31]. Hence, no extra power is required to maintain the graphene's conductivity at the desired value [45]. We realize the required amplitudes and phases of TF associated with spatial and temporal operations by combining the surface impedance model of a graphene monolayer to a transmission line (TL) approach. Several proof-of-principle examples are presented to demonstrate diverse wave-based signal processing functionalities like edge detection, complex spatial signal processing, temporal differentiation, and pulse spreading.

2. Theoretical Framework

First, we theoretically investigate the spatial and temporal optical transfer functions (OTFs) for different operations under normal and oblique incident waves. The OTF $\tilde{\mathbf{O}}(k_x, k_y, \Omega)$ ($\Omega = \omega - \omega_0$, ω_0 is the central frequency)

of **graphene-based multilayers** is the complex function that maps the incident electric field to the reflected/transmitted field. Let us consider a material-based processor located in the $x - y$ plane ($z = 0$). The incident and reflected fields, expressed in time domain, are denoted as $\psi^{in}(x, y, t)$ and $\psi^{out}(x, y, t)$ in a laboratory frame, respectively, where x and y are defined in the coordinate system of the beam, as shown in **Figure 1**. The OTF is written as a matrix to account for changes in the polarization of the reflected/transmitted light field.

We consider two channels: the spatial channel and the temporal channel (see **Figure 1**). These channels are separated by distinct polarizations or illumination angles; therefore, we can consider two OTFs, $\tilde{\mathbf{O}}^s(k_x, k_y)$ and $\tilde{\mathbf{O}}^t(\Omega)$, corresponding to the two channels, in spatial and temporal domains, respectively. In the paraxial regime, the incident beam has the form $\mathbf{P}^{in}\psi^{in}(x, y)$, where a 2-vector \mathbf{P}^{in} in the $x - y$ plane describes the input polarization, and $\psi^{in}(x, y)$ describes the scalar electric field distribution on the plane per-

pendicular to the beam propagation direction. In the spatial Fourier domain, each beam profile can be spectrally represented by a superposition of monochromatic plane waves, by Fourier transform:

$$\psi^{\text{in}}(x, y) = \int \int \tilde{\psi}^{\text{in}}(k_x, k_y) \exp(jk_x x + jk_y y) dk_x dk_y. \quad (1)$$

In addition, a similar equation can be considered for the temporal domain, as below,

$$\psi^{\text{in},t}(t) = \int \tilde{\psi}^{\text{in},t}(\Omega) \exp(j\Omega t) d\Omega. \quad (2)$$

Due to the tangential wavevector's continuity along with the interface, the incident spatial frequency component with (k_x, k_y) in the incident plane only generates the output spatial frequency component with the same (k_x, k_y) in the output plane. At each (k_x, k_y) , the output wave has an electric field of

$$\tilde{\Psi}^{\text{out}}(k_x, k_y) = \tilde{\mathbf{O}}^s(k_x, k_y) \cdot \mathbf{P}^{\text{in}} \tilde{\psi}^{\text{in}}(k_x, k_y), \quad (3)$$

where $\tilde{\mathbf{O}}^s(k_x, k_y)$ is 2×2 matrix (See [Appendix A](#)). The output beam passes through a polarizer selecting an output polarization \mathbf{P}^{out} , thereby an output electric field $\Psi^{\text{out}} = \mathbf{P}^{\text{out}} \psi^{\text{out}}(x, y)$; here, ψ^{out} , similar to ψ^{in} , is the field distribution on the output plane and has a spatial Fourier transform $\tilde{\psi}^{\text{out}}(k_x, k_y)$ in the (k_x, k_y) domain. Therefore, the relation between $\tilde{\psi}^{\text{out}}$ and $\tilde{\psi}^{\text{in}}$ is $\tilde{\psi}^{\text{out}}(k_x, k_y) = \tilde{\mathbf{O}}^s(k_x, k_y) \tilde{\psi}^{\text{in}}(k_x, k_y)$ where $\tilde{\mathbf{O}}^s(k_x, k_y) = \mathbf{P}^{\text{out} \dagger} \mathbf{O}^s(k_x, k_y) \mathbf{P}^{\text{in}}$.

Our desired OTF is the one corresponding to isotropic differentiation operation because it is one of the most fundamental operations in mathematics, and has several applications in engineering and image processing [37]. The TF of isotropic differentiation is $\tilde{\mathbf{O}}^s(k_x, k_y) = k_x^2 + k_y^2$, that must

have the obvious property $\tilde{\mathbf{O}}^s(k_x = 0, k_y = 0) = 0$. In our platform, one can achieve $\tilde{\mathbf{O}}^s(k_x = 0, k_y = 0) = 0$ by choosing the proper input and output polarizations such that

$$\mathbf{P}^{\text{out} \dagger} \mathbf{O}^s(k_x, k_y) \mathbf{P}^{\text{in}} = 0. \quad (4)$$

When the above equation is satisfied, the OTF in the vicinity of $k_x = k_y = 0$ has the below form (See [Appendix A](#)),

$$\tilde{\mathbf{O}}^s(k_x, k_y) = \gamma_1 k_x + \gamma_2 k_y. \quad (5)$$

In order to achieve two-dimensional homogeneous differentiation, the TF must have a rotationally invariant magnitude, and therefore $\gamma_2/\gamma_1 = \pm i$. The zeros of $\tilde{\mathbf{O}}^s(k_x, k_y)$ carry topological charge ± 1 . It means that after passing the Gaussian beam through the spatial differentiation system, the Gaussian beam will form a vortex light beam [57]. If the reflection coefficient for p- or s- polarized wave (r_{p0} and r_{s0}) is zero, the [Equation 4](#) is satisfied and by setting $\beta = \pi/2$, γ_2 and γ_1 can be calculated by (See [Appendix A](#))

$$\gamma_2 = \frac{\cot(\theta_0)}{k_0} r_{s0} P_y^{\text{in}}, \quad (6)$$

$$\gamma_1 = \frac{\partial r_p}{k_0 \partial \theta} P_x^{\text{in}}, \quad (7)$$

where $\mathbf{P}^{\text{in}} = (P_x^{\text{in}}, P_y^{\text{in}})^T$. Therefore, the output electric field distribution $\psi^{\text{out}}(x, y)$ will be proportional to $(\frac{\partial \psi^{\text{in}}}{\partial x} + i \frac{\partial \psi^{\text{in}}}{\partial y})$, as desired.

For the temporal channel, let us propose two distinct temporal processing: (i) performing the first-order temporal differentiation operation; and (ii), achieving temporal pulse spreading via a synthesized linear group-delay response at normal illumination (see [Figure 1](#)). In this channel, the input beam directly illuminates at normal illumination without using ro-

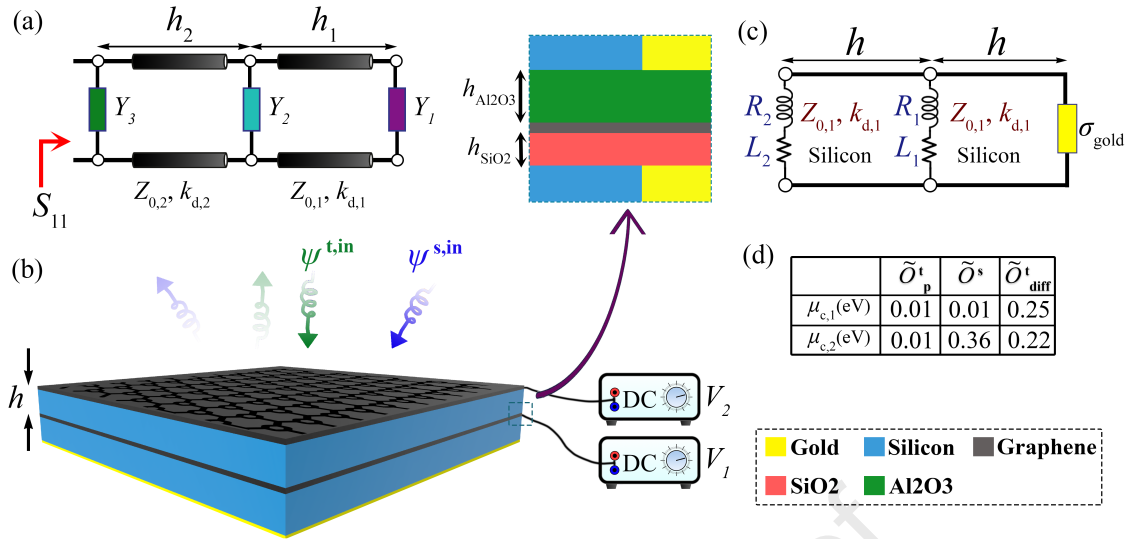


Figure 2: (a) Proposed TL model to achieve the desired reflection. (b) Schematic of the reconfigurable device and required layers for biasing the graphene monolayers. (c) Equivalent circuit model for the graphene-based computational multilayers. (d) Table of the required chemical potential of each graphene monolayer for a switchable scenario.

tation in the output polarization. Therefore, the OTF for the temporal channel can be defined as

$$\tilde{O}^t(\Omega) = \frac{\psi^{out,t}(\Omega)}{\psi^{in,t}(\Omega)}. \quad (8)$$

For temporal differentiator, the OTF can be represented as

$$\tilde{O}_{diff}^t(\Omega) = j\alpha\Omega. \quad (9)$$

Therefore, it is clear that the envelope of the temporally reflected/transmitted field with central frequency ω_0 has the field profile of

$$\psi_{diff}^{out}(t) = \alpha \frac{\partial \psi^{in,t}(t)}{\partial t}, \quad (10)$$

where α is a constant value.

In any temporal analog signal processor, there is a phaser, i.e., a two-port component with a TF exhibiting a group delay versus frequency response, which may be designed to show the group-delay (e.g., linear, quadratic, cubic, stepped, etc.) as core component [18]. One of the crucial applica-

tion of phaser is temporal pulse spreading via designing the linear group-delay response. The pulse-spreading operation allows us to steer the amplitude envelopes of quasi-sinusoid EM waves as desired, which is one of the basic impacts of temporal analog computing. In fact, input signal traveling along such a phaser experiences time spreading since its different spectral components travel with different group velocities, they temporally rearranged [7]. By exploiting this temporal rearrangement, the various spectral components of a signal can be directly mapped onto the time domain and can then be processed in a real-time manner. The group delay can be calculated via $\tilde{\tau}(\Omega) = -\frac{\partial}{\partial \omega} \text{Arg}\{\tilde{O}_p^t(\Omega)\}$; therefore, for linear group-delay response we can write:

$$\tilde{\tau}(\Omega) = -\frac{\partial}{\partial \omega} \text{Arg}\{\tilde{O}_p^t(\Omega)\} = a\Omega + b, \quad (11)$$

where a is the group-delay slope and b is constant. Consider the incident modulated Gauss pulse of duration T and bandwidth B , with central frequency ω_0 . As different spectral components of the Gauss pulse have different group delays when propagating through this phaser, the incident EM

pulse spreads over the time sequence, resulting in a broader reflected pulse with a duration of [41]

$$T' = T + \Delta\tau = T + aB = CT, \quad (12)$$

where $\Delta\tau$ is the group-delay swing over the frequency band B , and C represents the spreading factor of the spatial phaser. Additionally, the peak power of the reflected EM pulse is diminished to P_0/C . The schematic view of the proposed reconfigurable **multilayers** processor with the mentioned functionality in the spatial and temporal domain is illustrated in [Figure 1](#).

3. Graphene-Based **Multilayers** Design

We choose the surface impedance model for modeling of graphene-based multilayers, which represents a material-based system as an equivalent circuit model of specific configuration for realizing desired OTFs. The simple form of the proposed circuit model is illustrated in [Figure 2\(a\)](#). It contains three shunt admittances Y_1 , Y_2 , and Y_3 and two TLs of arbitrary lengths. In this model, the propagation constant of the guided mode along the TL is $k_d = k_0\sqrt{\epsilon_d - \sin^2\theta}$, where k_0 is the free space propagation constant, ϵ_d is permittivity of dielectric, and θ is the incident angle. The TL's characteristic impedance can be presented by Z_s and Z_p for the incidence wave polarized with s and p polarizations. We define characteristic impedances as $Z_s = \eta_0/\sqrt{\epsilon_d - \sin^2\theta}$, and $Z_p = \eta_0\sqrt{\epsilon_d - \sin^2\theta}/\epsilon_d$ for s and p polarizations, respectively, where η_0 indicates free space impedance. According to the utilized method, the TL matrix is given by [46]

$$\mathbf{T}_{TL} = \begin{bmatrix} \cos(k_d h) & jZ_d \sin(k_d h) \\ j\sin(k_d h)/Z_d & \cos(k_d h) \end{bmatrix}, \quad (13)$$

where h shows TL length and Z_d has to be replaced with the characteristic impedance of the TL with the considered polarization. In addition, a shunt admittance Y is introduced by the matrix below [46]:

$$\mathbf{T}_Y = \begin{bmatrix} 1 & 0 \\ Y & 1 \end{bmatrix}. \quad (14)$$

Then, the equivalent circuit matrix of the **graphene-based multilayers** is represented by

$$\mathbf{T}_C = \begin{bmatrix} T_{11} & T_{12} \\ T_{21} & T_{22} \end{bmatrix} = \mathbf{T}_{Y,3} \times \mathbf{T}_{TL,2} \times \mathbf{T}_{Y,2} \times \mathbf{T}_{TL,1} \times \mathbf{T}_{Y,1}. \quad (15)$$

Finally, the scattering matrix is calculated by [46]

$$\mathbf{S}_C = \begin{bmatrix} S_{11} & S_{12} \\ S_{21} & S_{22} \end{bmatrix} = \begin{bmatrix} \frac{T_{11}+T_{12}/Z_0-T_{21}Z_0-T_{22}}{T_{11}+T_{12}/Z_0+T_{21}Z_0+T_{22}} & \frac{2(T_{11}T_{22}-T_{12}T_{21})}{T_{11}+T_{12}/Z_0+T_{21}Z_0+T_{22}} \\ \frac{2}{T_{11}+T_{12}/Z_0+T_{21}Z_0+T_{22}} & \frac{-T_{11}+T_{12}/Z_0-T_{21}Z_0+T_{22}}{T_{11}+T_{12}/Z_0+T_{21}Z_0+T_{22}} \end{bmatrix}, \quad (16)$$

where Z_0 is the characteristics impedance of free space for the specific polarization considered, namely $Z_{0,s} = \eta_0/\cos\theta$ for s-polarization and $Z_{0,p} = \eta_0\cos\theta$ for p-polarization.

In order to implement the system, we propose a reflective graphene-based **multilayers** capable of switching between different states, depending on the illuminating beam. Graphene complex conductivity can be tuned by changing the Fermi level of graphene through electrical biasing or chemical doping. It is also practical to fabricate graphene-based structures with Complementary Metal-Oxide-Semiconductor (CMOS)

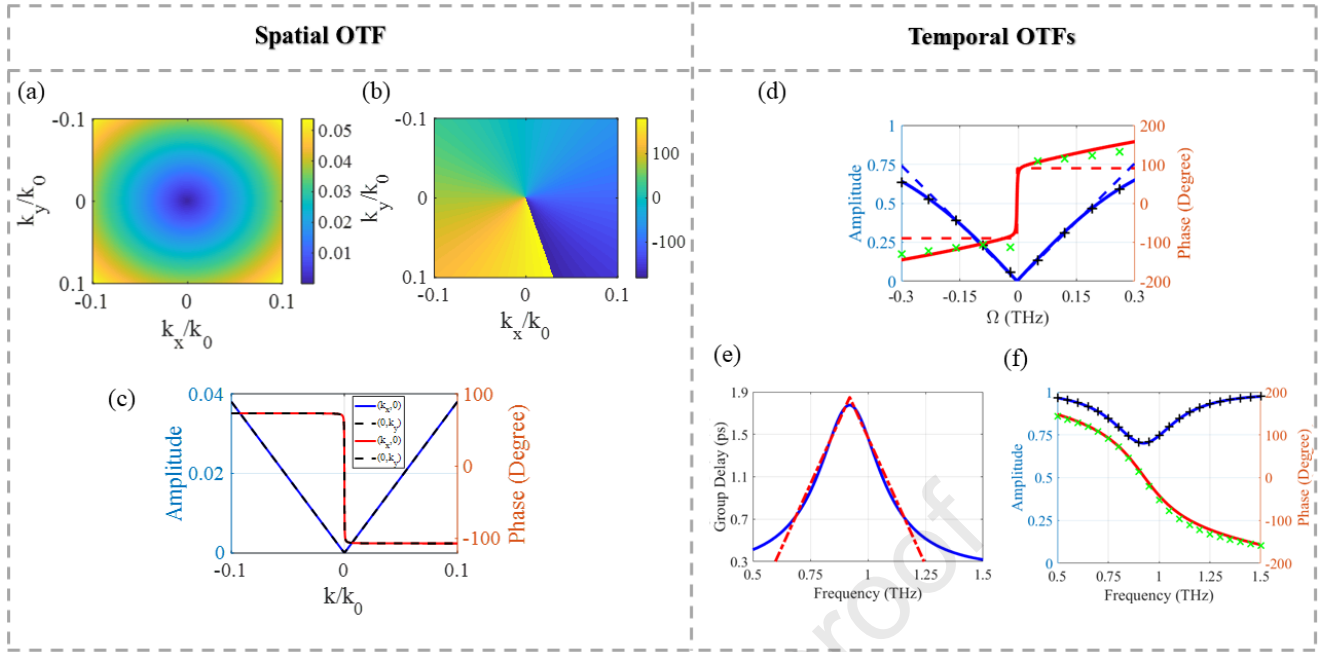


Figure 3: Synthesized Spatial and temporal OTF for different operations in the spatial (a,b) and temporal (d-f) channels. (a) Amplitude and (b) phase distribution of the spatial TF. (c) Comparison of amplitude and phase distribution in the $(k_x, 0)$ and $(0, k_y)$ planes. (d) Amplitude and phase of the OTF of the temporal differentiator. (e) Synthesized positive-triangular group delay and (f) amplitude and phase responses of the graphene-based phaser. The synthesized and ideal OTFs are indicated with solid and dashed lines, respectively. Black and green data points are generated independently, using the circuit model of the graphene-based multilayers.

technology as graphene is compatible with the required process [6]. In the model proposed in Figure 2(a), we assume Y_3 as a ground plane to stop transmission from the structure and design our material-based system in reflective mode, while TLs are used to model dielectric substrates. Graphene monolayers can represent the two other shunt admittances with different complex conductivity. Figure 2(c) shows a schematic representation of the TL model for the described structure.

According to graphene's outstanding features, we have utilized it as a tunable platform in a graphene-based **multi-layers** processor to switch between predetermined computational states. To start the design and perform an accurate evaluation of the proposed structure, graphene is modeled as an infinitesimally thin sheet with surface impedance $Z = 1/\sigma_g$, where σ_g is the frequency-dependent complex con-

ductivity of graphene. The surface conductivity of graphene including both intraband (σ_{intra}) and interband (σ_{inter}) transitions are governed by the well-known Kubo formula [19, 66]

$$\sigma_g(\omega, \tau, \mu_c, T) = \sigma_{intra}(\omega, \tau, \mu_c, T) + \sigma_{inter}(\omega, \tau, \mu_c, T), \quad (17)$$

$$\sigma_{intra}(\omega, \tau, \mu_c, T) = \quad (18)$$

$$-j \frac{e^2 k_B T}{\pi \hbar^2 (\omega - j\tau^{-1})} \left(\frac{\mu_c}{k_B T} + 2 \ln(e^{-\mu_c/k_B T} + 1) \right),$$

$$\sigma_{inter}(\omega, \tau, \mu_c, T) = -j \frac{e^2}{4\pi \hbar} \ln \left(\frac{2\mu_c - (\omega - j\tau^{-1})\hbar}{2\mu_c + (\omega - j\tau^{-1})\hbar} \right), \quad (19)$$

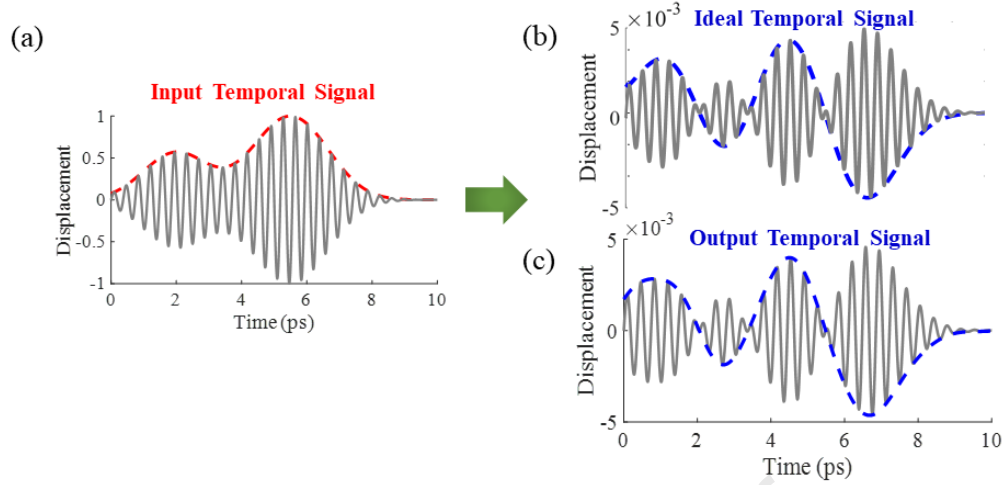


Figure 4: (a) The temporal envelope of the incident field is the input signal. (b) The ideal output we target, with its envelope representing the time derivative of the input signal. (c) Actual output, in very close agreement with the ideal output.

where e , \hbar , and k_B are constants corresponding to electron charge, the reduced Planck's constant, and the Boltzmann constant, respectively [19]. In the above equation, variables T , τ , and μ_c correspond to the environmental temperature, relaxation time, and the chemical potential of graphene, and ω is the angular frequency [19, 21]. In explaining graphene's optical response, the conical band diagram is essential for defining light-graphene interaction dynamics. Two types of band transitions are possible when a photon interacts with the graphene surface [42]. Depending on the relative positions of the Fermi level (E_f) and the energy of the incident photons, light absorption is either dominated by interband or intraband transitions, and the effects of these transitions are determined by Pauli blocking [15]. When the incident photon energy is lower than $2E_f$, intraband transitions become dominant, whereas in the opposite case, interband transitions dominate [35]. The interband conductivity is on the order of e^2/\hbar , and at frequencies below the THz regime and room temperatures, the interband term in complex conductivity is very small compared to the intraband term and usually can be ignored [19]. Moreover, graphene can be modeled as a thin dielectric. In this case the dielectric permittivity ϵ_g is

expressed as [50, 10]

$$\epsilon_g = 1 + j \frac{\sigma_g}{\epsilon_0 \omega \Delta_g}, \quad (20)$$

where Δ_g is the graphene thickness, and ϵ_0 is the vacuum permittivity. In a simple circuit model, we neglect the other parts of the floating-gate structure except for the graphene layer because their thickness is much smaller than a wavelength and their relative permittivities are similar to the ones of the nearby substrate. Hence, the floating-gate is modeled as a shunt impedance, and its value is equal to $1/\sigma_g$. In such a structure, the unpatterned graphene layer is a lossy medium that is represented through a series RL circuit in the demonstrated circuit model. **The frequency-dependent impedance is given by**

$$Z(\omega, \tau, \mu_c, T) = \frac{1}{\sigma} = R + j\omega L = \frac{\pi \hbar^2 (\omega - j2\Gamma)}{-je^2 k_B T \left(\frac{\mu_c}{k_B T} + 2 \ln(e^{-\mu_c/k_B T} + 1) \right)}. \quad (21)$$

So, the frequency-dependent inductance and resistance are calculated by

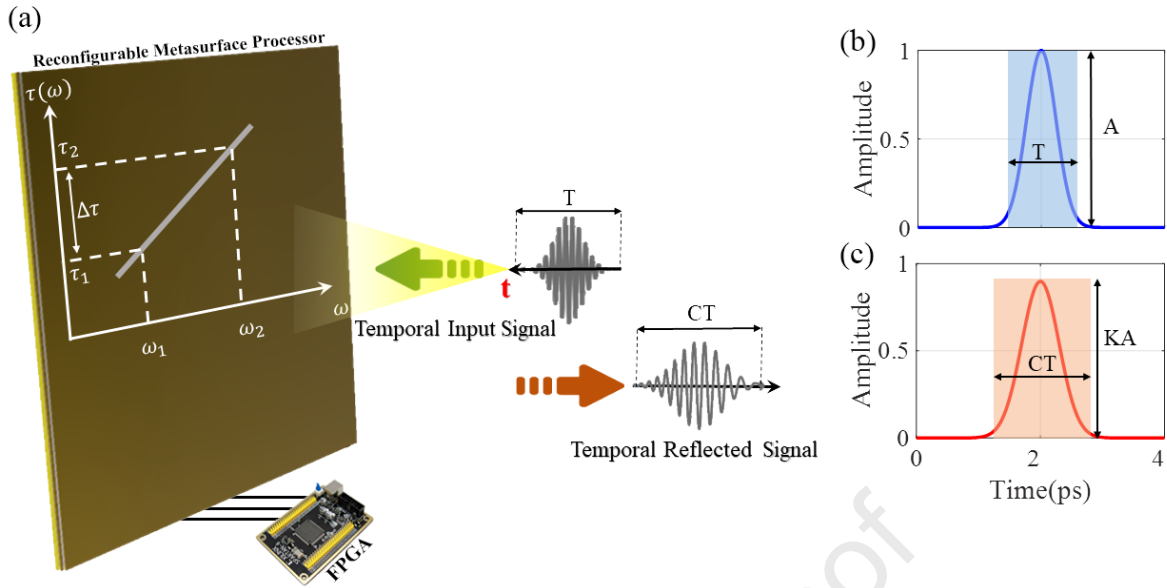


Figure 5: Temporal pulse spreading using a graphene-based multilayers processor. (a) Illustration of pulse spreading based on our graphene-based phaser with linear group-delay response. (b) Temporal envelope of the input signal and (c) temporal envelope of the output signal, scaled horizontally and vertically by factors C and K , respectively.

$$L(\omega, \tau, \mu_c, T) = \frac{\pi \hbar^2}{e^2 k_B T \left(\frac{\mu_c}{k_B T} + 2 \ln(e^{-\mu_c/k_B T} + 1) \right)}, \quad (22)$$

$$R(\omega, \tau, \mu_c, T) = \frac{\pi \hbar^2}{e^2 k_B T \tau \left(\frac{\mu_c}{k_B T} + 2 \ln(e^{-\mu_c/k_B T} + 1) \right)}. \quad (23)$$

By optimizing the TLs and graphene layer parameters, we can achieve the required behavior of the graphene-based multilayers. In this work, the environment temperature is considered to be $T = 300$ K. The proposed design consists of a fully covered graphene layer on top of a silicon substrate with a thickness of h and a metallic ground plane on the backside. In this composition, the relative permittivity and loss tangent of the silicon substrate are $\epsilon_{r, Si} = 11.9$ and

$\tan \delta = 0.00025$. The same structure consisting of a silicon substrate and an unpatterned graphene layer with different electrostatic bias is embedded upon the primary segment. Additionally, the designed graphene-based multilayers processor is very stable versus perturbation in environmental temperature. We assume the same TLs in both sections, but we can use different TLs with different materials and lengths if more degrees of freedom were required for the target functionality. Indeed, by using the same TLs, we decreased the number of optimized parameters and reduced the computational load of the optimization process. We numerically simulate the design in CST Studio Suite to get the reflection amplitude and phase. The amplitude and phase control in the graphene-based multilayers is achieved via changes in its complex conductivity controlled by an external voltage on the floating-gates, which changes the chemical potential.

In most prior research works, a simple capacitive structure consisting of graphene, an insulator, and a metallic electrode is used to tune graphene's conductivity. However, the disadvantage of this method is that an external driven voltage

must be applied continually to sustain graphene's conductivity. Consequently, static power consumption is inevitable. In order to resolve this drawback, we propose a **graphene-based multilayers** with nearly zero static power consumption based on a non-volatile floating-gate graphene structure as widely used in some non-volatile devices [52, 31, 32]. This structure consists of Si, SiO₂, Al₂O₃, and graphene monolayers, as illustrated in [45]. The selected biasing configuration for the **graphene-based multilayers** is depicted schematically in **Figure 2(b)**. In the graphene unpatterned layers, μ_c can be tuned by adjusting the charge density of graphene n as given by [59]

$$\mu_c = \text{sgn}(n) \hbar v_F \sqrt{(\pi |n|)} \quad (24)$$

where $v_F = 10^6$ m/s is the Fermi velocity [67]. We employ a floating-gate structure to tune the charge density of the graphene. The floating-gate design is widely used in some non-volatile devices [26]. In the floating-gate design, when a voltage is applied on the top Si layer, the electrons in the bottom Si layer can tunnel through the SiO₂ and been captured by the graphene, increasing its charge density. In this case, we assumed the voltage on the top Si layer is positive. On the contrary, when the reverse voltage is applied on the top Si layer, the electrons in graphene can tunnel through the SiO₂ and been captured by the bottom Si layer, so the charge density is decreased [45]. In this design, the graphene monolayer is isolated electrically from the Si layers, which means after removing the voltage, the charge density of graphene can remain constant for an extended period of time. So, in this structure, no extra power is needed to keep charge density consistent. The thickness of the Al₂O₃ and SiO₂ are $h_{\text{Al}_2\text{O}_3} = 20$ nm, and $h_{\text{SiO}_2} = 10$ nm, respectively. Therefore, the electrons can only tunnel through the SiO₂ layer, whereas they cannot tunnel through the Al₂O₃ layer

because its thickness is much larger compared to the SiO₂ layer. Also, the relative permittivity of the Al₂O₃ layer is $\epsilon_{r,\text{Al}_2\text{O}_3} = 9$, and the relative permittivity of SiO₂ is $\epsilon_{r,\text{SiO}_2} = 3.9$ [53]. These ultrathin layers are important to consider in the design of the DC bias but can be neglected in the Thz simulations. The charge density of graphene is expressed as the integral of tunneling current J_{SiO_2} in the SiO₂, which is given by

$$n = \frac{1}{e} \int_0^{t_0} J_{\text{SiO}_2} dt, \quad (25)$$

where t_0 is the duration of the voltage applied on the Si. The tunneling current according to the Fowler-Nordheim tunneling mechanism is given by [29]

$$J_{\text{SiO}_2} = \frac{e^3}{16\pi^2 \hbar \phi_{\text{SiO}_2}} E_{\text{SiO}_2}^2 \exp\left(-\frac{4(2m)^{1/2} \phi_{\text{SiO}_2}^{3/2}}{3\hbar e E_{\text{SiO}_2}}\right) \quad (26)$$

In the above equation, $\phi_{\text{SiO}_2} = 3.2$ eV is the barrier height of SiO₂, E_{SiO_2} shows the electric field in SiO₂, and m indicates effective mass of electron. The electric field in SiO₂ is expressed by

$$E_{\text{SiO}_2} = \frac{V_g}{h_{\text{SiO}_2} + h_{\text{Al}_2\text{O}_3} (\epsilon_{r,\text{SiO}_2} / \epsilon_{r,\text{Al}_2\text{O}_3})} - \frac{en}{\epsilon_{r,\text{SiO}_2} [1 + (\epsilon_{r,\text{Al}_2\text{O}_3} h_{\text{SiO}_2}) / (\epsilon_{r,\text{SiO}_2} h_{\text{Al}_2\text{O}_3})]} \quad (27)$$

where V_g indicates the applied voltage to the graphene layer. Using the Kubo formula and voltage-dependent property of floating-gate, the required external voltage for a specific value of chemical potential is calculated in **Appendix B**. When the voltage on the top Si layer is positive, the value of σ_g increases by voltage. When the voltage is negative, the value of σ_g decreases with the reverse voltage. Finally, after removing the voltage, the value of σ_g remains constant, and no

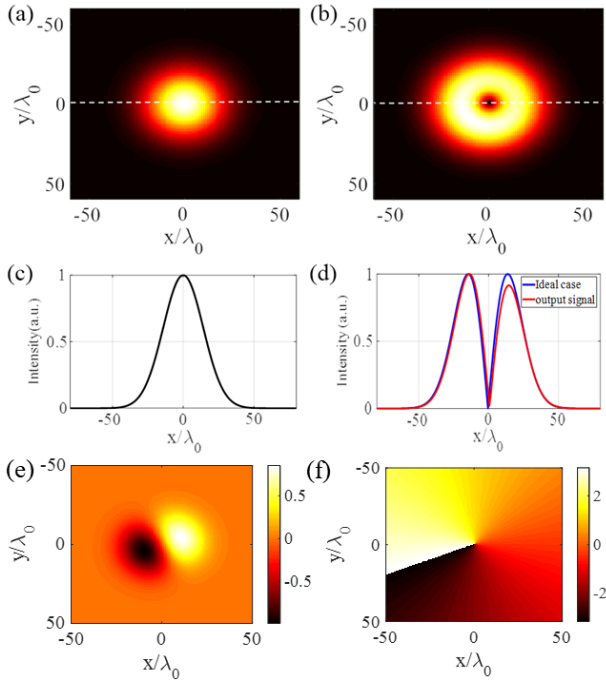


Figure 6: Spatial differentiation on an input Gaussian beam and generation of a vortex beam. Intensity distribution of the (a) incident and (b) reflected fields. (c) Intensity distribution of the incident field along the dashed lines in (a). (d) Intensity distribution of the output field along the dashed lines in (b). The ideal and output signals have also been illustrated for the sake of comparison in (d). (e) and (f) The real part and phase of reflected fields, respectively.

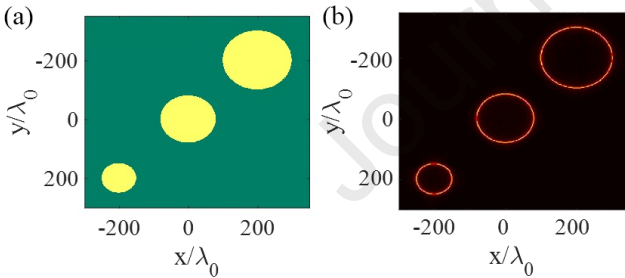


Figure 7: Edge detection of a 2-dimensional image by exploiting the proposed graphene-based multilayers processor. (a) Input and (b) the edge-detected images, respectively.

voltage is needed to sustain σ_g . Hence, the floating-gate tuning design is preferred to the capacitor-based tuning methods, where the static power consumption is inevitable [13, 48].

4. Results and Discussion

As we discussed in the above section, we modeled reconfigurable graphene-based multilayers by leveraging a TL

approach to synthesize desired OTFs in spatial and temporal domains. In fact, we engineered the temporal- and spatial-frequency response of the proposed graphene-based multilayers by fine-tuning the scattering parameters of Equation 16. We defined a cost function, $F = ||\text{OTF}^{\text{des}}(k_x/k_y, \Omega) - \text{OTF}^{\text{syn}}(k_x/k_y, \Omega)||$, and searched for a set of circuit parameters which ensures $F \rightarrow 0$, where OTF^{des} is our desired OTF and OTF^{syn} is S_{11} in Equation 16. A particle swarm optimization (PSO) algorithm [11] is adopted to minimize the value of F .

4.1. Switchable Analog Computing Performance

This section wants to investigate a switchable graphene-based multilayers that can switch between determined operations in the desired channel (temporal or spatial). In this scenario, the relaxation time of graphene is assumed to be $\tau = 0.08$ ps, and the dielectric thickness is $h = 12$ μm . The required chemical potential for graphene monolayers to achieve the desired functionality- isotropic spatial differentiation, temporal differentiation and linear group-delay response- is illustrated in Figure 2(d). We numerically simulate the design in CST Studio Suite to get the reflection amplitude and phase. The obtained results show that the graphene-based multilayers supports both spatial and temporal channels, which can be selected by applying a proper external electrostatic voltage. To explicitly present the properties of the synthesized graphene-based multilayers processor, the spatial and temporal OTFs as a function of the incidence angle and temporal frequency are illustrated in Figure 3. The obtained results are exactly what we explained in Section 2 and the theoretical calculations, which are calculated based on the TL approach in Section 3 are in excellent agreement with simulated results. The left side of Figure 3 represents the spatial OTF for isotropic differentiation operation. The input polarization can be computed by Equations 6 and 7 and

the fact that $\gamma_2/\gamma_1 = i$. The operating frequency for the spatial channel is 1 THz and $\theta_0 = 22.3^\circ$. Based on Equation 5, we have the helical phase distribution of the spatial TF in Figure 3(b) as we expected from Equation 5. The amplitude and phase of OTF for $(k_x, 0)$ and $(0, k_y)$ are plotted in Figure 3(c). This is evidence that two-dimensional edge detection can be achieved properly. The right side of Figure 3 shows the temporal OTFs associated with first-order differentiation operation and linear group delay response. Figure 3(d) exhibits the amplitude and phase of the synthesized OTF associated with first-order temporal differentiation. For ease of comparison, the ideal case and TL approach results are also plotted in this figure. The bandwidth of the temporal channel is $|\Omega/\omega_0| < 0.25$. This range essentially provides the maximum temporal resolution of input signals that can be correctly processed by the designed graphene-based multilayers. Finally, the triangular group delay response is plotted in Figure 3(e) and its amplitude and phase are also sketched in Figure 3(f).

Let us consider the temporal channel. By tuning the chemical potentials, $\mu_{c,1}$ and $\mu_{c,2}$ expressed in Figure 2(d), the graphene-based multilayers processor can act as a temporal differentiator. To explicitly demonstrate the functionality of temporal differentiation with the designed graphene-based multilayers, we investigate the applications of simulated results in Figure 3(d) on 1D temporal signals. First, we calculated the frequency spectra input signal of Figure 4(a) with Fourier transform. After that, the output signal could be computed by Equation 2. As standard outputs, we have presented the results processed with the ideal temporal first-order derivation in Figure 4(b). By comparing the output result in Figure 4(c) with the ideal differentiated signal in Figure 4(b), excellent agreement is observed.

We now move to the phaser, which provides a desired

group-delay response over a given frequency band [41]. For an incident EM wave that has various sinusoidal components, it has the form

$$\psi^{in,t}(t) = \sum_{n=0}^{N-1} A_n(t) \cdot e^{j\omega_n t + \phi_n}. \quad (28)$$

Thus, the output EM wave has the form of [9]

$$\psi^{out,t}(t) = |\tilde{O}_p^t| \sum_{n=0}^{N-1} A_n(t - \tilde{\tau}(\omega_n)) \cdot e^{j\omega_n t + \phi(\omega_n) + \phi_n}. \quad (29)$$

From the above equation, we can observe that the amplitude envelopes of different sinusoidal components have different time delays depending on their frequencies. Figure 5 shows the process to realize pulse spreading through a linear group-delay response graphene-based multilayers phaser. An incident modulated Gauss pulse of duration T (the time range of 10% peak amplitude) and bandwidth B , with central frequency ω_0 , is radiated to the graphene-based multilayers-based phaser. As we can see in Figure 3(e), the group delay has a positive slope (approximately $0.85 \text{ ps}^2/\text{rad}$) from 0.65 to 0.95 THz, and a negative slope from 0.94 to 1.25 THz. Based on Equation 12, the predicted spreading time is $\Delta\tau = aB = 0.7 \text{ ps}$. As we can see in Figures 5(b) and (c), the synthesized linear group delay leads to 0.7 ps spreading time duration of input temporal signal. The values of C and $K = 1/\sqrt{C}$ are 1.57 and 0.8, respectively.

We now switch to the spatial channel at an oblique incident angle, at which the graphene-based graphene-based multilayers performs isotropic spatial differentiation. We first consider the scenario where the input is a Gaussian beam, as shown in Figures 6(a) and (c). The operator in Equation 5, operating on an input Gaussian beam, produces a beam with a vortex-shaped beam that possesses a donut-shaped intensity profile (see Figure 6(b)). The real part and phase of reflected fields are demonstrated in Figures 6(e) and (f).

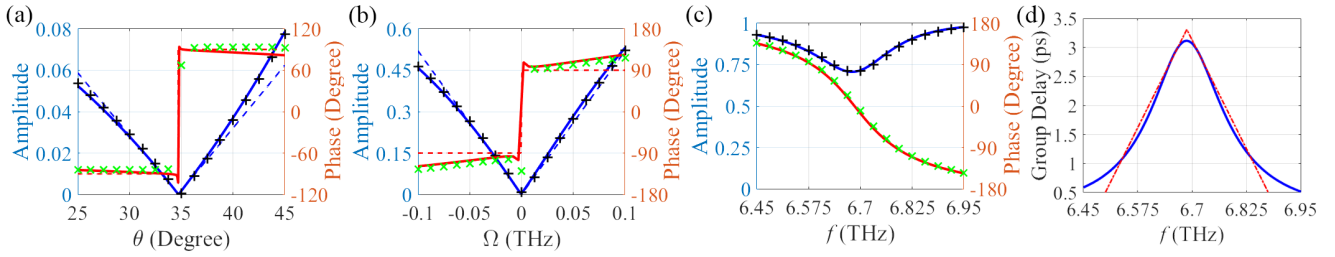


Figure 8: Synthesized Spatial and temporal OTF for parallel spatiotemporal computing. (a) Amplitude (blue) and phase (red) of the spatial TF associated with the spatial differentiation operation. (b) Amplitude (blue) and phase (red) of the temporal TF associated with the temporal differentiation operation. (c) Amplitude (blue) and phase (red) distribution of synthesized **graphene-based multilayers** for linear group-dealy response. (d) Synthesized positive-triangular group delay. The synthesized and ideal OTFs are indicated with solid and dashed lines, respectively. Also, green and black cross lines are related to the results of TL model of the graphene-based **multilayers**.

For the sake of comparison, we also plot the ideal normalized magnitude of a differentiated Gaussian beam in [Figure 6\(d\)](#), indicating a great performance of the differentiation.

Edge detection, as advanced applications of analog optical computing in image processing, plays a crucial role in image segmentation and in other basic image pre-processing steps. We now investigate it with an input image consisting of three distinct circular shapes, which is shown in [Figure 7\(a\)](#). The reflected images are numerically simulated, and the corresponding transverse field profiles are displayed in [Figure 7\(b\)](#). As expected, the isotropic spatial edge-detector **graphene-based multilayers** successfully reveals all outlines of the obliquely incident image along the vertical and horizontal orientations. The **graphene-based multilayers** shows acceptable results for edge detection according to illustrated results in [Figure 7](#). **The operating function of the designed devices can be altered between predetermined operators with reasonable speed. The proper investigation of switching speed is presented in Appendix C. Also, the reconfigurable processor can be programmed by using external processor as explained in Appendix D.**

4.2. Simultaneous Spatiotemporal Analog Computing Performance

Here, we investigate another opportunity, namely to perform parallel analog spatiotemporal computing, with the proposed graphene-based **graphene-based multilayers**. Our motivation is the potential enhancement of channel bandwidth by expanding the analog computing from the single spatial or temporal operation to parallel spatiotemporal operation [71, 64].

Consider the scenario in which temporal and spatial channels are simultaneously excited by spatial and temporal signals at different angles as well as frequencies. Similar to the previous section, we consider first-order spatial differentiation as a spatial operation and first-order temporal differentiation as well as linear group-delay response as temporal functions. In this scenario, graphene's relaxation time is considered as $\tau = 0.06$ ps, and the substrates thickness are $h = 18\mu\text{m}$. The required chemical potential for graphene monolayers to achieve the desired functionality is $\mu_{c,1} = \mu_{c,2} = 0.32$ eV. [Figure 8](#) provides the results of parallel computing including spatial and temporal TFs. [Figures 8\(a\) and \(b\)](#) show the spaial and temporal OTFs associated with first-order differentiation operation, respectively. The operating frequency for the temporal channel is 1.9 THz and $\theta_0 = 34.6^\circ$. Also, the center frequency of the spatial chan-

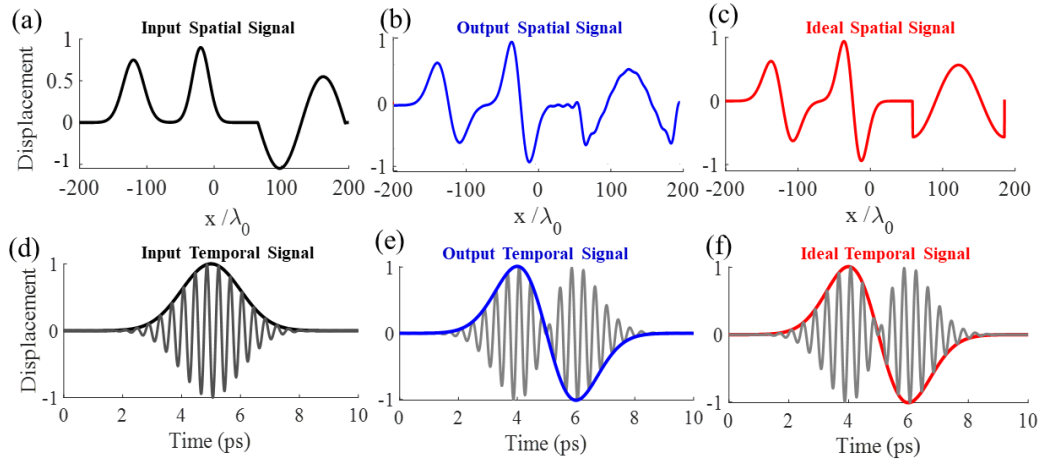


Figure 9: (a) The complex input field profile is the combination of Gaussian and sinusoidal functions. We compare (b) the output signal envelope to (c) the exact derivative of the input signal envelope. The signals are normalized to one. (d) A Gaussian pulse is used as an input in the time domain. (e) and (f) The normalized output and ideal temporal signals, respectively.

nel is 0.65 THz and $\theta_0 = 34.6^\circ$. Similar to the previous section, the ideal case and TL method results are also plotted in same figures. The bandwidth for spatial and temporal channels are $|k/k_0| < 0.2$ and $|\Omega/\omega_0| < 0.1$. Figure 8(c) exhibits the amplitude and phase of synthesized OTF associated with linear group delay response of Figure 8(d). From Figure 8(d), the group delay has a positive slope from 6.45 to 6.7 THz and vice-versa a negative slope from 6.7 to 6.95 THz.

A complex signal which is a combination of Gaussian and sinusoidal functions (see Figure 9(a)), has been utilized as the beam profile of incidence. The corresponding results, including output signal and an ideal case, are illustrated in Figures 9(b) and (c). In addition, we adopt a Gaussian pulse for temporal differentiation as the input signal (see Figure 9(d)). The output signal and an ideal case, are demonstrated in Figures 9(e) and (f). As can be seen, the graphene-based multilayers successfully implements the spatio-temporal differentiation of the input signal.

5. Conclusion

To conclude, we exploited a novel switchable subwavelength architecture for optical analog computing of spatiotem-

poral and simultaneous computing. The proposed graphene-based multilayers is compact without the need for optical Fourier transform elements, where optical computation functions are directly achieved in the real space rather than the Fourier space. By leveraging the surface impedance model of graphene layers and using the TL approach, the computational graphene-based multilayers for temporal and spatial processing with a proper spatial and temporal bandwidth was engineered. In the temporal channel, first-order differentiation and graphene-based multilayers phaser for temporal pulse spreading application via synthesizing linear group-delay response are demonstrated. Besides, in the spatial channel, performing isotropic differentiation operation as well as edge detection are provided. According to the floating-gate design utilized in this paper, the external voltage can be removed after biasing the graphene layers according to the desired function. We have eventually validated the spatial and temporal differentiation with one-dimensional spatial/temporal signals and an image, with excellent agreement between full-wave numerical simulations and targetted operations.

Acknowledgment: A. Momeni and R. Fleury acknowl-

edge funding from the Swiss National Science Foundation under the Eccellenza grant number 181232.

A. Appendix A: Calculation of Spatial

Transfer Function

We define $\mathbf{P}^{in} = (P_x^{in}, P_y^{in})^T$ and $\mathbf{P}^{out} = (P_x^{out}, P_y^{out})^T$ as the normalized input and output polarizations in x-y plane, respectively.

The TF $\tilde{O}^s(k_x, k_y) = \mathbf{P}^{out\dagger} \mathbf{O}^s(k_x, k_y) \mathbf{P}^{in}$ can be written as [73, 57]

$$\tilde{O}^s(k_x, k_y) = \mathbf{P}^{out\dagger} \mathbf{V}_2^\dagger \mathbf{R}^s(k_x, k_y) \mathbf{V}_1 \mathbf{P}^{in}, \quad (30)$$

where

$$\begin{aligned} \mathbf{R}^s(k_x, k_y) &= \begin{bmatrix} r_p & 0 \\ 0 & r_s \end{bmatrix}, \\ \mathbf{V}_1 &= \begin{bmatrix} 1 & \zeta \\ -\zeta & 1 \end{bmatrix}, \\ \mathbf{V}_2 &= \begin{bmatrix} -1 & -\zeta \\ -\zeta & 1 \end{bmatrix}, \end{aligned} \quad (31)$$

where the matrices \mathbf{V}_1 and \mathbf{V}_2 are originated from the rotations of coordinates and $\zeta = \cot(\theta_0)k_y/k_0$. Also, the r_p and r_s are the Fresnel coefficients for p- and s- polarized plane waves, respectively. According to Equation 4 in main text, and Equation 30 in ($k_x = 0, k_y = 0$) we have

$$-r_{p0} P_x^{in} P_x^{out*} + r_{s0} P_y^{in} P_y^{out*} = 0, \quad (32)$$

where, the r_{p0} , and r_{s0} are the Fresnel coefficients for p- and s- polarized plane waves at the incident angle θ_0 , respectively. By approximating the Fresnel reflection coefficients with first-order Taylor expansions ($r_{p/s} = r_{p0/s0} + \frac{\partial r_{p/s}}{\partial \theta} k_x/k_0$) [73, 57], and after some straightforward mathe-

matical manipulations, the coefficients γ_1 and γ_2 in Equation 5 are found as:

$$\begin{aligned} \gamma_1 &= \frac{1}{k_0} \left(-P_x^{in} P_x^{out*} \frac{\partial r_p}{\partial \theta} + P_y^{in} P_y^{out*} \frac{\partial r_s}{\partial \theta} \right), \\ \gamma_2 &= -\frac{\cot(\theta_0)}{k_0} \left(-P_y^{in} P_x^{out*} + P_x^{in} P_y^{out*} \right) (r_{p0} + r_{s0}). \end{aligned} \quad (33)$$

In the case of operating at oblique incidence (with $r_{p0} = 0$), by setting $\beta = \pi/2$, the expressions for the coefficients γ_1 and γ_2 collapse to Equations 6 and 7 of the main text.

B. Appendix B: Electrostatic voltages

By solving Equations 24, 25, 26, and 27, we can calculate the required voltage for biasing the graphene monolayer. This section will calculate the time response of chemical potential for different applied voltages to the floating-gate panel. According to Figure 10(a), when the applied voltage on the top Si layer is positive, the electric field intensity in SiO2 and tunneling current increase, resulting in more electrons tunneling through the SiO2 layer and captured by the graphene. Accordingly, the chemical potential of the graphene layer increases with time [45]. By applying $V_{FG} = 30V$ to the structure, the desired range of chemical potential can be achieved. Also, when the applied voltage on the top Si layer is negative, the electric field in SiO2 reverses, leading to more electrons tunneling through the SiO2 layer and going back to the bottom Si layer [45]. Consequently, the chemical potential of the graphene layer is decreased, as shown in Figure 10(b). By applying $V_{FG} = -20V$ to the structure, the value of chemical potential required for the designs presented in this paper can be obtained.

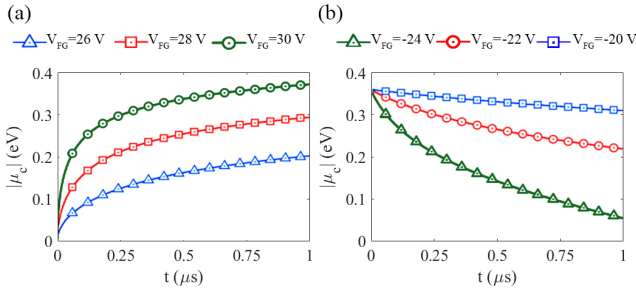


Figure 10: The time response of chemical potential where (a) positive and (b) reverse voltages are applied to the floating-gate panel.

C. Appendix C: Computing and Switching

Speed

In the proposed reconfigurable processor, two different types of speeds need to be considered: (1) computing speed and (2) switching speed.

(1) Computing speed: For each operation, computing speed (for both temporal and spatial) is very high due to the nature of the THz electromagnetic waves used for computing.

(2) Switching speed: Switching speed is related to the speed of switching between different operations.

The switching speed depends on several parameters, such as the external bias circuit's time constant (RC), the speed of graphene reaction to the bias change as a function of relaxation time, and the time response of chemical potential. The total relaxation time depends on different scattering mechanisms at different carrier densities and temperatures. The Matthiessen rule defines the overall relaxation time τ_t for any given carrier density n and temperature T [3],

$$\frac{1}{\tau_t} \simeq \frac{1}{\tau_L} + \frac{1}{\tau_S}. \quad (34)$$

where τ_L is due to long-range scattering mechanisms, such as defects and impurities, and τ_S is due to short-range scattering mechanisms, such as phonon and carrier-carrier interactions [3]. The total resistance and the total capacitance of the biasing circuit can help us to control the biasing speed.

Reducing the resistance of graphene/metal contact and capacitance enables a fast switching speed. Recent progress in graphene fabrication and low-resistance contacts may allow speeds of up to hundreds of GHz [3]. A lower resistance value can be achieved by properly adjusting the graphene/metal contacts as long as they do not deteriorate the reflective structure's reflection phase and amplitude spectra. As another solution, to reduce resistance, more efficient ohmic contacts can be devised. In addition, the switching speed between different operational states is limited by the operating frequency of field-programmable gate array (FPGA) that is about a few GHz [17]. Ultimately, the time response of the chemical potential variation is the limiting parameter. As already explained in Appendix B, in the worst-case scenario, the chemical potential of the graphene monolayer can be switched from the highest required value to the minimum value in 1 μs . So, the switching speed between different chemical potentials is about a few MHz. This speed is high enough to allow for our principal goal here, which is to switch between different operational states in a matter of seconds.

D. Appendix D: External Biasing

In Figure 2(a), V_1 and V_2 are tunable DC gate voltages that can control the Fermi energy level, which helps to control the complex surface conductivity of the graphene monolayers easily. The Fermi energy level experiences a sufficient variation covering our region of interest while the voltage is reasonably changed. The required DC voltage bias can be applied to each graphene monolayer via gold contacts. In addition, an FPGA hardware can be exploited to provide the desired electrostatic voltages at its output pins and set the operational status of each layer independently. Consequently, proper switching among different states can be reg-

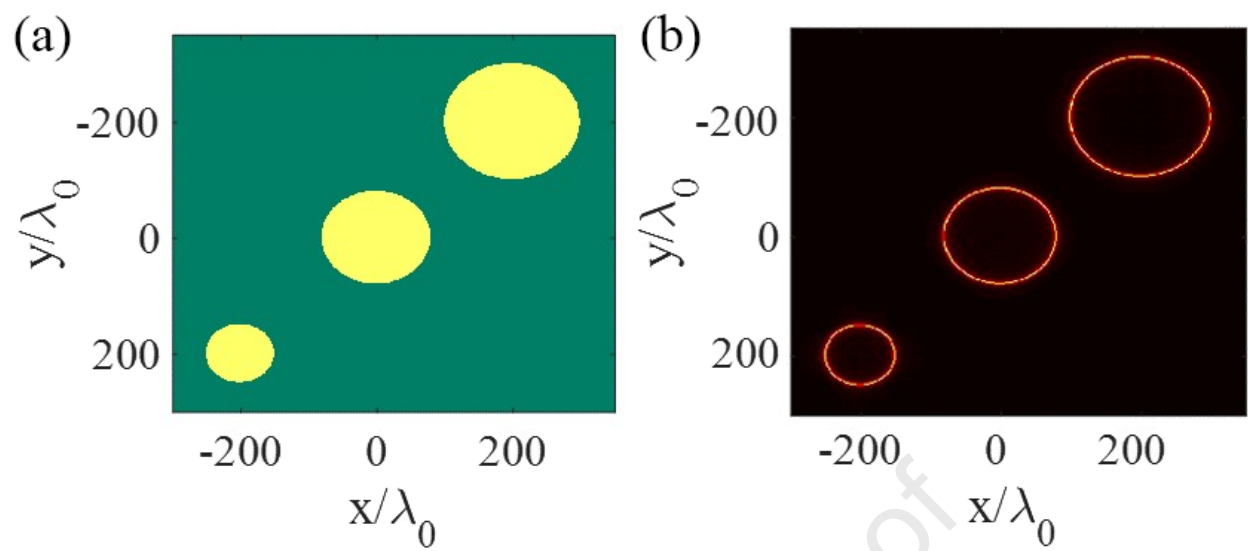
istered into the internal memory of the FPGA, which enables different operation states for the device.

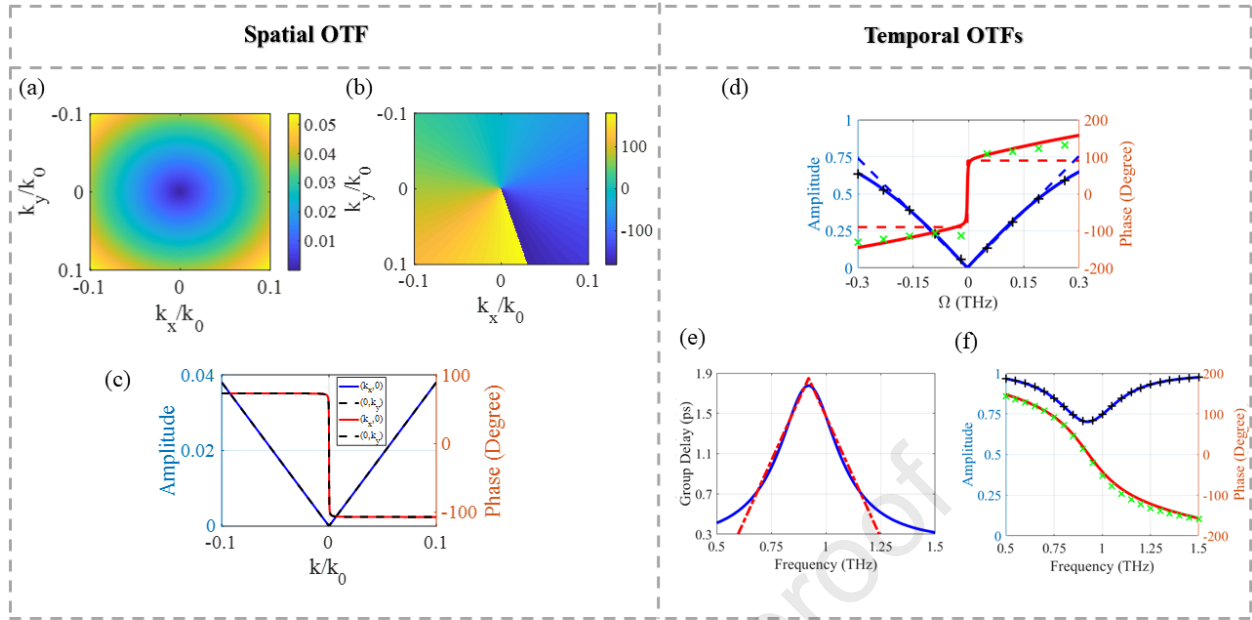
References

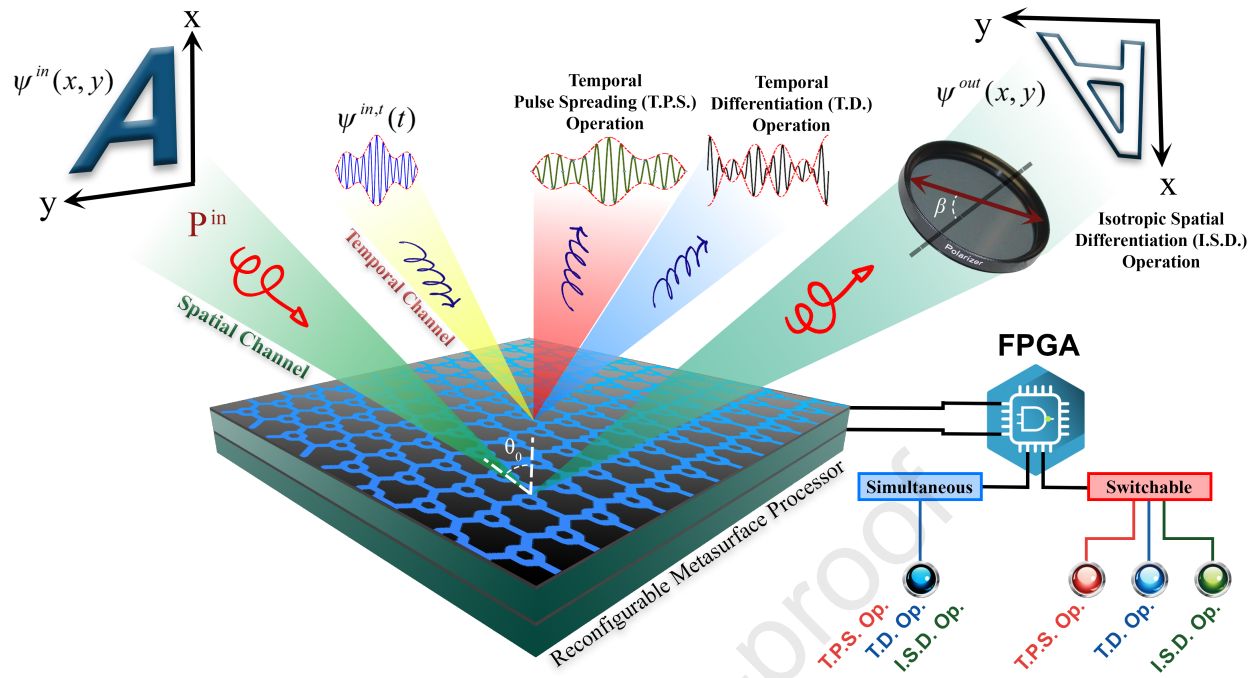
- [1] Abdolali, A., Momeni, A., Rajabalipanah, H., Achouri, K., 2019. Parallel integro-differential equation solving via multi-channel reciprocal bianisotropic metasurface augmented by normal susceptibilities. *New Journal of Physics* 21, 113048.
- [2] Abdollahramezani, S., Hemmatyar, O., Adibi, A., 2020. Meta-optics for spatial optical analog computing. *Nanophotonics* 9, 4075–4095.
- [3] Alvarez, C.N., Cheung, R., Thompson, J.S., 2017. Performance analysis of hybrid metal–graphene frequency reconfigurable antennas in the microwave regime. *IEEE Transactions on Antennas and Propagation* 65, 1558–1569.
- [4] Babaee, A., Momeni, A., Abdolali, A., Fleury, R., 2021. Parallel analog computing based on a 2×2 multiple-input multiple-output metasurface processor with asymmetric response. *Physical Review Applied* 15, 044015.
- [5] Babaee, A., Momeni, A., Moeini, M.M., Fleury, R., Abdolali, A., 2020. Parallel optical spatial signal processing based on 2×2 mimo computational metasurface, in: 2020 Fourteenth International Congress on Artificial Materials for Novel Wave Phenomena (Metamaterials), IEEE. pp. 195–197.
- [6] Banerjee, S.K., Register, L.F., Tutuc, E., Basu, D., Kim, S., Reddy, D., MacDonald, A.H., 2010. Graphene for cmos and beyond cmos applications. *Proceedings of the IEEE* 98, 2032–2046.
- [7] Caloz, C., Gupta, S., Zhang, Q., Nikfal, B., 2013. Analog signal processing: A possible alternative or complement to dominantly digital radio schemes. *IEEE Microwave Magazine* 14, 87–103.
- [8] Chen, D., Yang, J., Huang, J., Bai, W., Zhang, J., Zhang, Z., Xu, S., Xie, W., 2019. The novel graphene metasurfaces based on splitting resonators for tunable polarization switching and beam steering at terahertz frequencies. *Carbon* 154, 350–356.
- [9] Chen, M.Z., Cheng, Q., Xia, F., Rashid, A.K., Dai, J.Y., Zhang, C., Zhang, Q., Cui, T.J., 2020a. Metasurface-based spatial phasers for analogue signal processing. *Advanced Optical Materials* 8, 2000128.
- [10] Chen, X., Zhang, J., Wen, C., Liu, K., Zhu, Z., Qin, S., Yuan, X., 2020b. Optical nonlinearity and non-reciprocal transmission of graphene integrated metasurface. *Carbon* 173, 126–134.
- [11] Eberhart, R., Kennedy, J., 1995. Particle swarm optimization, in: *Proceedings of the IEEE international conference on neural networks*, Citeseer. pp. 1942–1948.
- [12] Estakhri, N.M., Edwards, B., Engheta, N., 2019. Inverse-designed metastructures that solve equations. *Science* 363, 1333–1338.
- [13] Fallah, S., Rouhi, K., Abdolali, A., 2019. Optimized chemical potential graphene-based coding metasurface approach for dynamic manipulation of terahertz wavefront. *Journal of Physics D: Applied Physics* 53, 085102.
- [14] Ferrera, M., Park, Y., Razzari, L., Little, B.E., Chu, S.T., Morandotti, R., Moss, D., Azaña, J., 2010. On-chip cmos-compatible all-optical integrator. *Nature Communications* 1, 29.
- [15] Grigorenko, A., Polini, M., Novoselov, K., 2012. Graphene plasmonics. *Nature photonics* 6, 749–758.
- [16] Guo, C., Xiao, M., Minkov, M., Shi, Y., Fan, S., 2019. Optical computing using photonic crystal slabs, in: *Photonic and Phononic Properties of Engineered Nanostructures IX*, International Society for Optics and Photonics. p. 109270Y.
- [17] Guo, J.R., You, C., Zhou, K., Goda, B.S., Kraft, R.P., McDonald, J.F., 2003. A scalable 2 v, 20 ghz fpga using sige hbt bicmos technology, in: *Proceedings of the 2003 ACM/SIGDA eleventh international symposium on Field programmable gate arrays*, pp. 145–153.
- [18] Gupta, S., Parsa, A., Perret, E., Snyder, R.V., Wenzel, R.J., Caloz, C., 2010. Group-delay engineered noncommensurate transmission line all-pass network for analog signal processing. *IEEE transactions on microwave theory and techniques* 58, 2392–2407.
- [19] Hanson, G.W., 2008. Dyadic green's functions for an anisotropic, non-local model of biased graphene. *IEEE Transactions on antennas and propagation* 56, 747–757.
- [20] He, S., Zhou, J., Chen, S., Shu, W., Luo, H., Wen, S., 2020. Spatial differential operation and edge detection based on the geometric spin hall effect of light. *Optics Letters* 45, 877–880.
- [21] Hosseinienejad, S.E., Rouhi, K., Neshat, M., Cabellos-Aparicio, A., Abadal, S., Alarcón, E., 2019a. Digital metasurface based on graphene: An application to beam steering in terahertz plasmonic antennas. *IEEE Transactions on Nanotechnology* 18, 734–746.
- [22] Hosseinienejad, S.E., Rouhi, K., Neshat, M., Faraji-Dana, R., Cabellos-Aparicio, A., Abadal, S., Alarcón, E., 2019b. Re-programmable graphene-based metasurface mirror with adaptive focal point for thz imaging. *Scientific reports* 9, 1–9.
- [23] Hou, J., Dong, J., Zhang, X., 2017. Optical solver for a system of ordinary differential equations based on an external feedback assisted microring resonator. *Optics Letters* 42, 2310–2313.

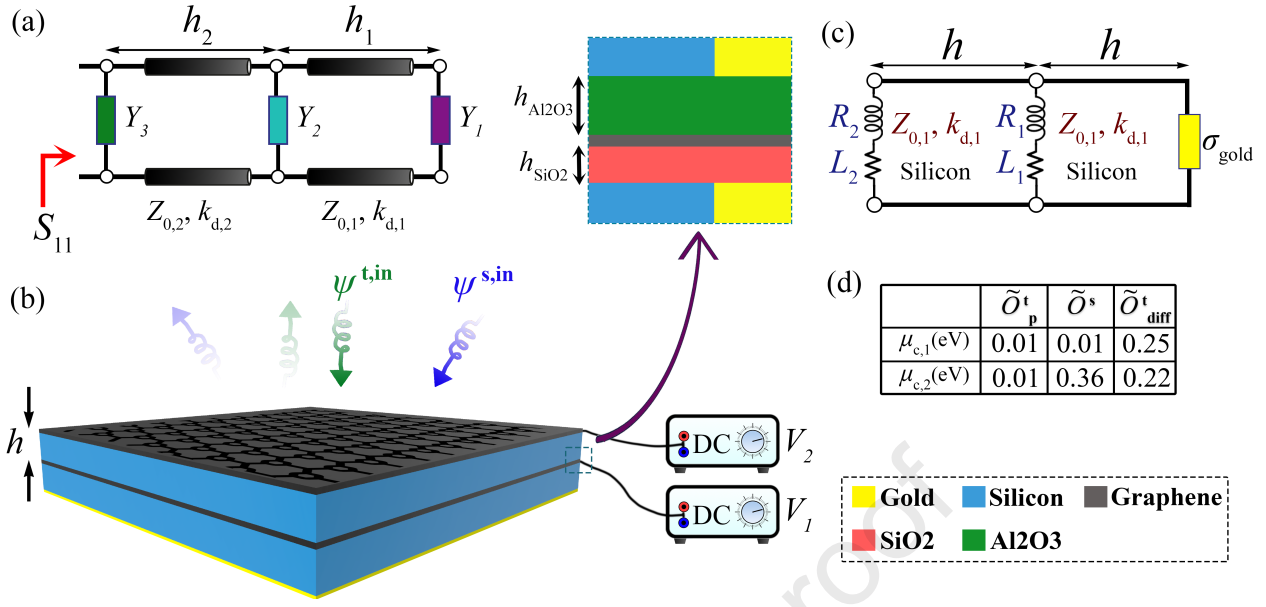
- [24] Huo, P., Zhang, C., Zhu, W., Liu, M., Zhang, S., Zhang, S., Chen, L., Lezec, H.J., Agrawal, A., Lu, Y., et al., 2020. Photonic spin-multiplexing metasurface for switchable spiral phase contrast imaging. *Nano Letters* 20, 2791–2798.
- [25] Islam, M., Sultana, J., Biabanifard, M., Vafapour, Z., Nine, M., Dinovitsner, A., Cordeiro, C., Ng, B.H., Abbott, D., 2020. Tunable localized surface plasmon graphene metasurface for multiband super-absorption and terahertz sensing. *Carbon* 158, 559–567.
- [26] Jang, S., Hwang, E., Lee, J.H., Park, H.S., Cho, J.H., 2015. Graphene-graphene oxide floating gate transistor memory. *Small* 11, 311–318.
- [27] Karimi, A., Zarifkar, A., Miri, M., 2019. Subpicosecond flat-top pulse shaping using a hybrid plasmonic microring-based temporal differentiator. *JOSA B* 36, 1738–1747.
- [28] Kiani, M., Momeni, A., Tayarani, M., Ding, C., 2020. Spatial wave control using a self-biased nonlinear metasurface at microwave frequencies. *Optics Express* 28, 35128–35142.
- [29] Lenzlinger, M., Snow, E., 1969. Fowler-nordheim tunneling into thermally grown sio₂. *Journal of Applied physics* 40, 278–283.
- [30] Li, J., Li, J., Zheng, C., Wang, S., Li, M., Zhao, H., Li, J., Zhang, Y., Yao, J., 2021. Dynamic control of reflective chiral terahertz metasurface with a new application developing in full grayscale near field imaging. *Carbon* 172, 189–199.
- [31] Li, Y., Yu, H., Dai, T., Jiang, J., Wang, G., Yang, L., Wang, W., Yang, J., Jiang, X., 2015. Graphene-based floating-gate nonvolatile optical switch. *IEEE Photonics Technology Letters* 28, 284–287.
- [32] Li, Y., Yu, H., Qiu, X., Dai, T., Jiang, J., Wang, G., Zhang, Q., Qin, Y., Yang, J., Jiang, X., 2018. Graphene-based nonvolatile terahertz switch with asymmetric electrodes. *Scientific reports* 8, 1–9.
- [33] Liu, W., Li, M., Guzzon, R.S., Norberg, E.J., Parker, J.S., Lu, M., Coldren, L.A., Yao, J., 2016. A fully reconfigurable photonic integrated signal processor. *Nature Photonics* 10, 190–195.
- [34] Lu, W.B., Wang, J.W., Zhang, J., Liu, Z.G., Chen, H., Song, W.J., Jiang, Z.H., 2019. Flexible and optically transparent microwave absorber with wide bandwidth based on graphene. *Carbon* 152, 70–76.
- [35] Mak, K.F., Ju, L., Wang, F., Heinz, T.F., 2012. Optical spectroscopy of graphene: From the far infrared to the ultraviolet. *Solid State Communications* 152, 1341–1349.
- [36] Momeni, A., Fleury, R., 2021. Wave-based extreme deep learning based on non-linear time-floquet entanglement. *arXiv preprint arXiv:2107.08564*.
- [37] Momeni, A., Rajabalipanah, H., Abdolali, A., Achouri, K., 2019. Generalized optical signal processing based on multioperator metasurfaces synthesized by susceptibility tensors. *Physical Review Applied* 11, 064042.
- [38] Momeni, A., Rajabalipanah, H., Rahmzadeh, M., Abdolali, A., Achouri, K., Asadchyk, V., Fleury, R., 2020. Reciprocal metasurfaces for on-axis reflective optical computing. *arXiv preprint arXiv:2012.12120*.
- [39] Momeni, A., Rouhi, K., Rajabalipanah, H., Abdolali, A., 2018. An information theory-inspired strategy for design of re-programmable encrypted graphene-based coding metasurfaces at terahertz frequencies. *Scientific reports* 8, 1–13.
- [40] Momeni, A., Safari, M., Abdolali, A., Kherani, N.P., Fleury, R., 2021. Asymmetric metal-dielectric metacylinders and their potential applications from engineering scattering patterns to spatial optical signal processing. *Physical Review Applied* 15, 034010.
- [41] Nikfal, B., Badiere, D., Repeta, M., Deforge, B., Gupta, S., Caloz, C., 2012. Distortion-less real-time spectrum sniffing based on a stepped group-delay phaser. *IEEE microwave and wireless components letters* 22, 601–603.
- [42] Ozdemir, O., Aygar, A.M., Balci, O., Kocabas, C., Caglayan, H., Ozbay, E., 2016. Enhanced tunability of v-shaped plasmonic structures using ionic liquid gating and graphene. *Carbon* 108, 515–520.
- [43] Pan, K., Leng, T., Song, J., Ji, C., Zhang, J., Li, J., Novoselov, K.S., Hu, Z., 2020. Controlled reduction of graphene oxide laminate and its applications for ultra-wideband microwave absorption. *Carbon* 160, 307–316.
- [44] Pandian, G.S., Seraji, F.E., 1991. Optical pulse response of a fibre ring resonator. *IEE Proceedings J (Optoelectronics)* 138, 235–239.
- [45] Peng, X.L., Hao, R., Chen, W., Chen, H.s., Yin, W.Y., Li, E.P., 2017. An active absorber based on nonvolatile floating-gate graphene structure. *IEEE Transactions on Nanotechnology* 16, 189–195.
- [46] Pozar, D.M., 2011. *Microwave engineering*. John wiley & sons.
- [47] Qi, L., Liu, C., Shah, S.M.A., 2019. A broad dual-band switchable graphene-based terahertz metamaterial absorber. *Carbon* 153, 179–188.
- [48] Rajabalipanah, H., Rouhi, K., Abdolali, A., Iqbal, S., Zhang, L., Liu, S., 2020. Real-time terahertz meta-cryptography using polarization-multiplexed graphene-based computer-generated holograms. *Nanophotonics* 9, 2861–2877.
- [49] Rouhi, K., Rajabalipanah, H., Abdolali, A., 2018. Real-time and broadband terahertz wave scattering manipulation via polarization-

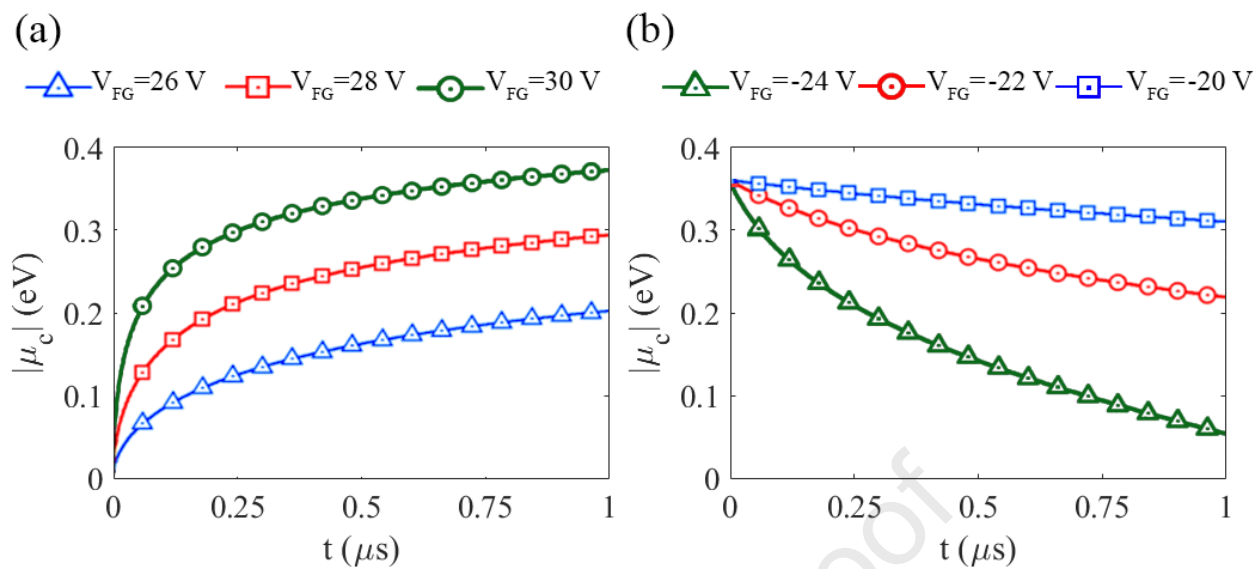
- insensitive conformal graphene-based coding metasurfaces. *Annalen der Physik* 530, 1700310.
- [50] Rouhi, K., Rajabalipanah, H., Abdolali, A., 2019. Multi-bit graphene-based bias-encoded metasurfaces for real-time terahertz wavefront shaping: From controllable orbital angular momentum generation toward arbitrary beam tailoring. *Carbon* 149, 125–138.
- [51] Silva, A., Monticone, F., Castaldi, G., Galdi, V., Alù, A., Engheta, N., 2014. Performing mathematical operations with metamaterials. *Science* 343, 160–163.
- [52] Wang, X., Xie, W., Xu, J.B., 2014. Graphene based non-volatile memory devices. *Advanced Materials* 26, 5496–5503.
- [53] Wilk, G.D., Wallace, R.M., Anthony, J., 2001. High- κ gate dielectrics: Current status and materials properties considerations. *Journal of applied physics* 89, 5243–5275.
- [54] Wu, D., Wang, M., Feng, H., Xu, Z., Liu, Y., Xia, F., Zhang, K., Kong, W., Dong, L., Yun, M., 2019. Independently tunable perfect absorber based on the plasmonic properties in double-layer graphene. *Carbon* 155, 618–623.
- [55] Wu, J., Cao, P., Hu, X., Jiang, X., Pan, T., Yang, Y., Qiu, C., Tremblay, C., Su, Y., 2014. Compact tunable silicon photonic differential-equation solver for general linear time-invariant systems. *Optics express* 22, 26254–26264.
- [56] Xiao, S., Wang, T., Liu, T., Yan, X., Li, Z., Xu, C., 2018. Active modulation of electromagnetically induced transparency analogue in terahertz hybrid metal-graphene metamaterials. *Carbon* 126, 271–278.
- [57] Xu, D., He, S., Zhou, J., Chen, S., Wen, S., Luo, H., 2020. Optical analog computing of two-dimensional spatial differentiation based on the Brewster effect. *Optics Letters* 45, 6867–6870.
- [58] Xu, W., Xie, L., Zhu, J., Tang, L., Singh, R., Wang, C., Ma, Y., Chen, H.T., Ying, Y., 2019. Terahertz biosensing with a graphene-metamaterial heterostructure platform. *Carbon* 141, 247–252.
- [59] Yan, J., Zhang, Y., Kim, P., Pinczuk, A., 2007. Electric field effect tuning of electron-phonon coupling in graphene. *Physical review letters* 98, 166802.
- [60] Yang, T., Dong, J., Lu, L., Zhou, L., Zheng, A., Zhang, X., Chen, J., 2014. All-optical differential equation solver with constant-coefficient tunable based on a single microring resonator. *Scientific reports* 4, 5581.
- [61] Yi, N., Liu, Z., Sun, S., Song, Q., Xiao, S., 2015. Mid-infrared tunable magnetic response in graphene-based diabolical nanoantennas. *Carbon* 94, 501–506.
- [62] Zangeneh-Nejad, F., Fleury, R., 2019. Topological analog signal processing. *Nature communications* 10, 1–10.
- [63] Zangeneh-Nejad, F., Sounas, D.L., Alù, A., Fleury, R., 2020. Analogue computing with metamaterials. *Nature Reviews Materials* , 1–19.
- [64] Zhang, J., Ying, Q., Ruan, Z., 2019. Time response of plasmonic spatial differentiators. *Optics letters* 44, 4511–4514.
- [65] Zhang, Y., Feng, Y., Jiang, T., Cao, J., Zhao, J., Zhu, B., 2018a. Tunable broadband polarization rotator in terahertz frequency based on graphene metamaterial. *Carbon* 133, 170–175.
- [66] Zhang, Y., Feng, Y., Zhao, J., 2020. Graphene-enabled tunable multifunctional metamaterial for dynamical polarization manipulation of broadband terahertz wave. *Carbon* .
- [67] Zhang, Y., Tan, Y.W., Stormer, H.L., Kim, P., 2005. Experimental observation of the quantum hall effect and Berry's phase in graphene. *nature* 438, 201–204.
- [68] Zhang, Z., Yan, X., Liang, L., Wei, D., Wang, M., Wang, Y., Yao, J., 2018b. The novel hybrid metal-graphene metasurfaces for broadband focusing and beam-steering in farfield at the terahertz frequencies. *Carbon* 132, 529–538.
- [69] Zhou, J., Qian, H., Chen, C.F., Zhao, J., Li, G., Wu, Q., Luo, H., Wen, S., Liu, Z., 2019. Optical edge detection based on high-efficiency dielectric metasurface. *Proceedings of the National Academy of Sciences* 116, 11137–11140.
- [70] Zhou, J., Qian, H., Zhao, J., Tang, M., Wu, Q., Lei, M., Luo, H., Wen, S., Chen, S., Liu, Z., 2020a. Two-dimensional optical spatial differentiation and high-contrast imaging. *Natl. Sci. Rev.* .
- [71] Zhou, Y., Zhan, J., Chen, R., Chen, W., Wang, Y., Shao, Y., Ma, Y., 2021. Analogue optical spatiotemporal differentiator. *Advanced Optical Materials* , 2002088.
- [72] Zhou, Y., Zheng, H., Kravchenko, I.I., Valentine, J., 2020b. Flat optics for image differentiation. *Nature Photonics* 14, 316–323.
- [73] Zhu, T., Huang, J., Ruan, Z., 2020. Optical phase mining by adjustable spatial differentiator. *Advanced Photonics* 2, 016001.
- [74] Zhu, T., Zhou, Y., Lou, Y., Ye, H., Qiu, M., Ruan, Z., Fan, S., 2017. Plasmonic computing of spatial differentiation. *Nature communications* 8, 1–6.

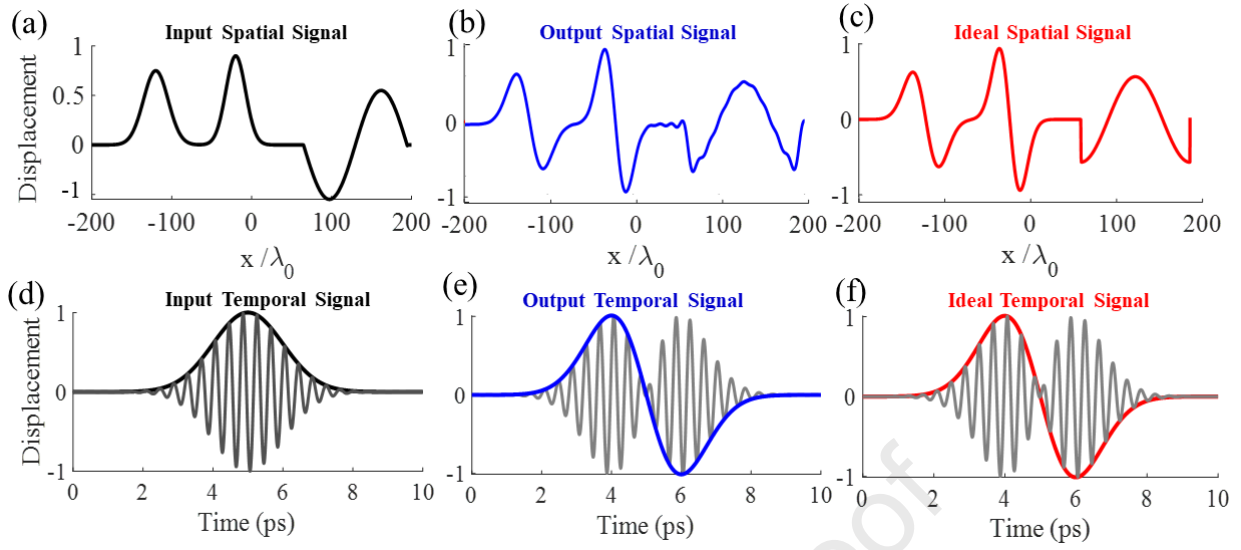




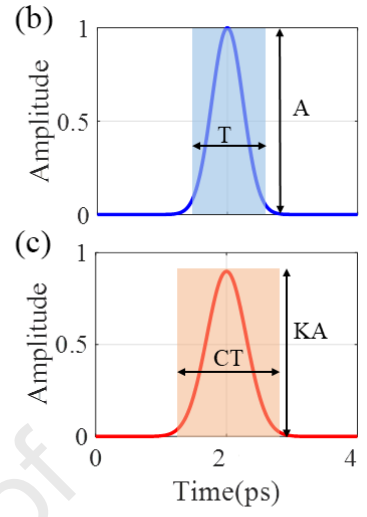
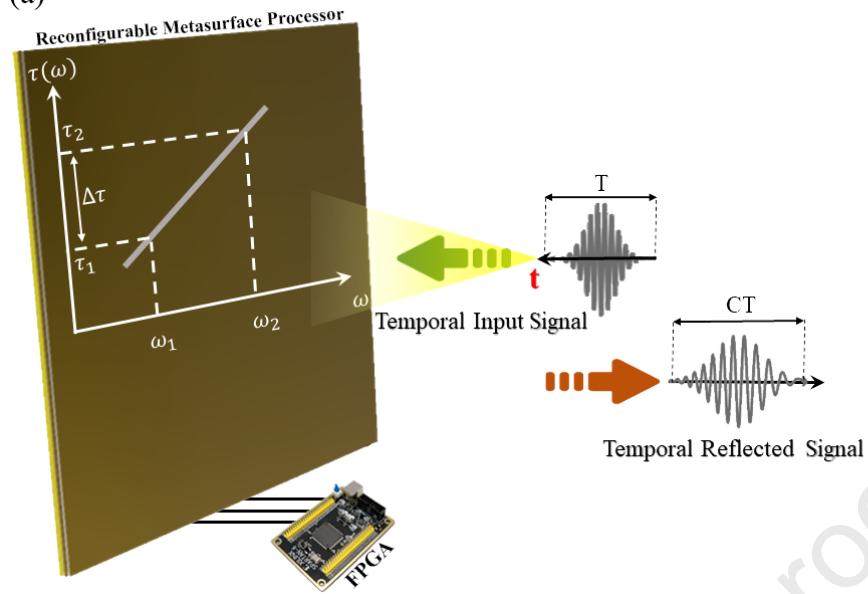


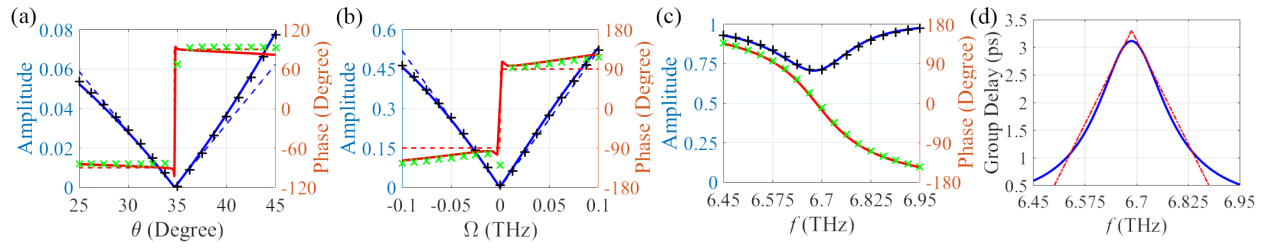




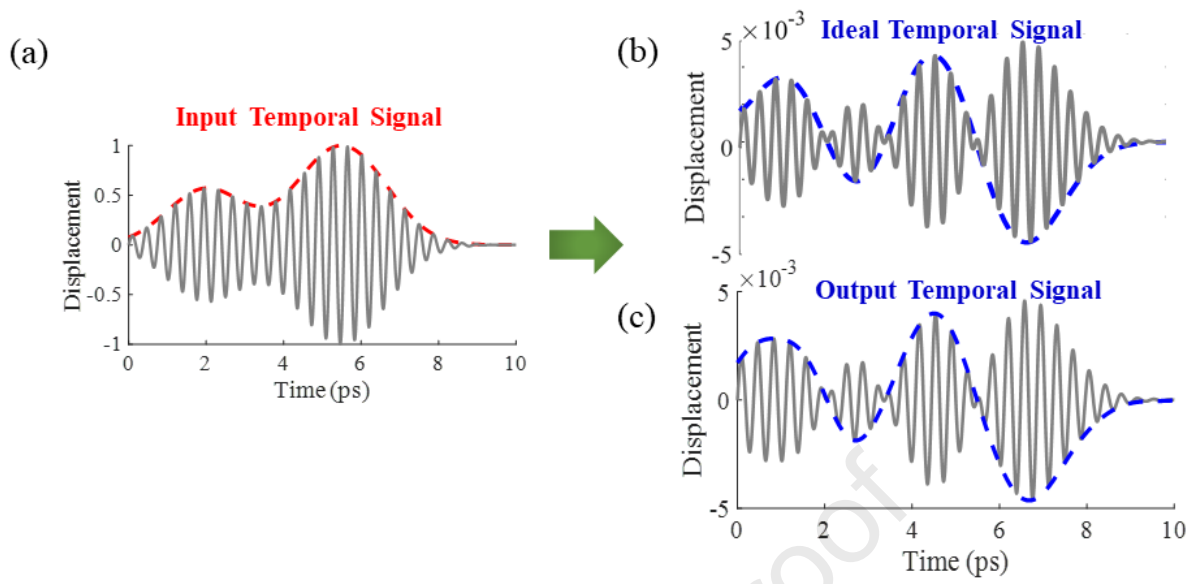


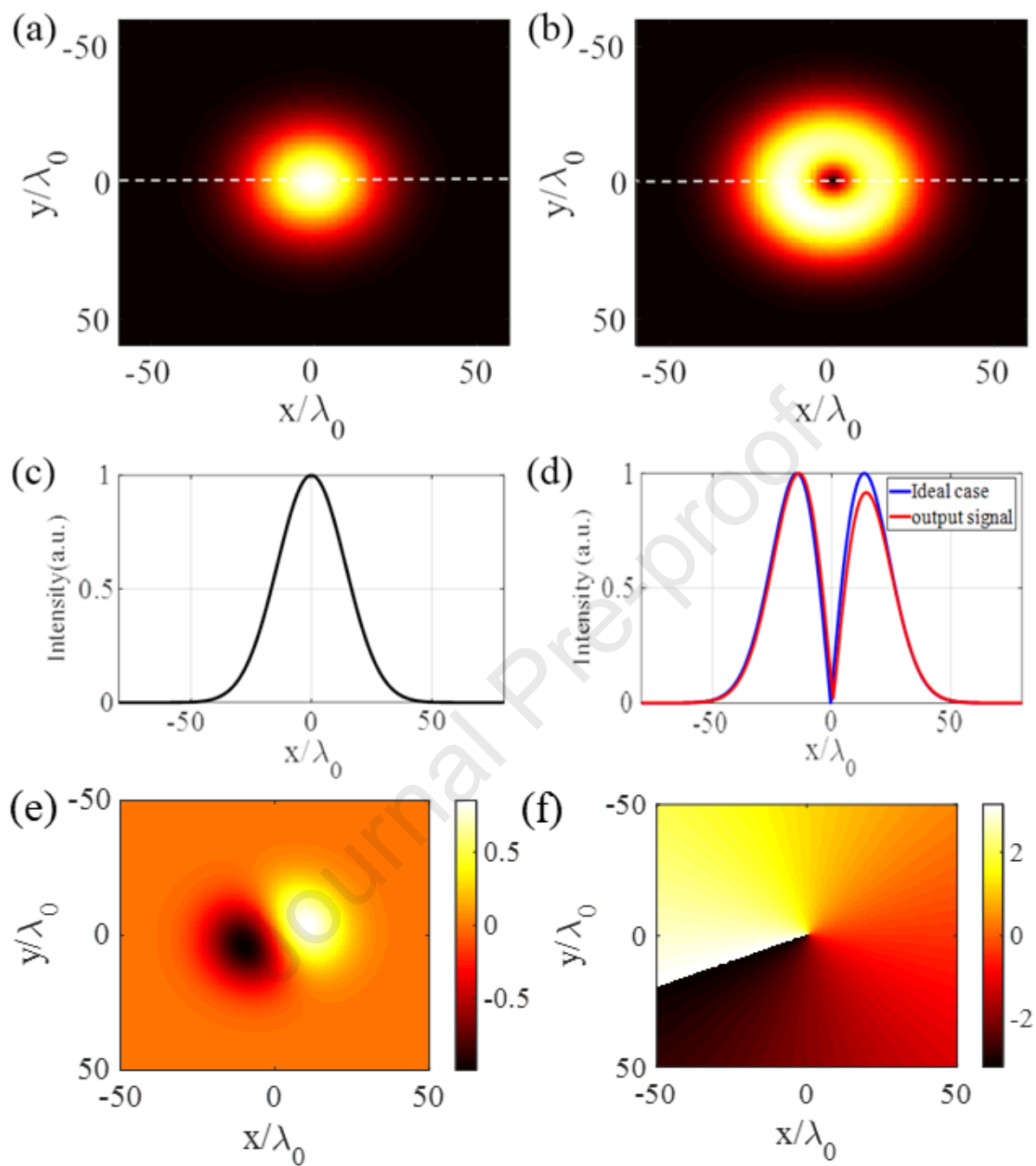
(a)





Journal Pre-proof





Declaration of interests

The authors declare that they have no known competing financial interests or personal relationships that could have appeared to influence the work reported in this paper.

The authors declare the following financial interests/personal relationships which may be considered as potential competing interests:

Journal Pre-proof